EES Catalysis

PAPER

Published on 08 August 2026

Cite this: DOI: 10.1039/d6ey00123h

Accelerated hydrogen peroxide production in sonicated emulsive water microdroplets using short-chain alcohols as interfacial additives

Gavin Hazen, †[ab] Shi Li, †[d] Sonam Rani, †[ab] Hung V. Nguyen, [bc] Ethan Gilhuly, [ab] Fabiola Rangel,[ab] Abdelilah Asserghine, [a] Charles M. Schroeder,‡[bc] Rajeev S. Assary [d] and Joaquín Rodríguez-López *[ab]

Water microdroplets generated through ultrasonication of water/oil systems spontaneously produce hydrogen (H_2) and hydrogen peroxide (H_2O_2) under ambient, catalyst-free conditions, offering a potential route towards decentralized redox chemistry. However, product yields remain low and the origins of interfacial reactivity and selectivity remain poorly understood. Here, we show that short-chain alcohols provide a simple and powerful molecular handle to amplify the redox chemistry of sonicated emulsive water microdroplets (SEWMs), enabling enhanced and controllable production of up to 60 mM H_2O_2 and 2 mM H_2 within 30 minutes of ultrasonication under catalyst-free conditions. Alcohol identity and concentration strongly modulate SEWM size distributions, droplet populations, and redox activity, with short-chain primary alcohols significantly enhancing reactivity whereas long-chain, substituted alcohols suppress this effect. We further demonstrate that redox product selectivity can be tuned by modifying the local gaseous environment, with oxygen-rich conditions favoring H_2O_2 production and oxygen-free conditions promoting H_2 evolution. We reveal how alcohols provide redox pathways to the millimolar production of CO_2, CO, and CH_4, as well as various water-soluble, organic products, including formic acid, acetic acid, and methanediol. Molecular dynamics simulations reveal that alcohols modify the water/oil droplet interface, disrupting the interfacial hydrogen bonding networks and order of the oil phase, thereby enhancing local electric fields and fluctuations in the local dipole orientations. Collectively, these results establish alcohol-containing SEWMs as redox rich, tunable, catalyst-free microreactors for on-demand redox chemistry.

Received 2nd June 2026,
Accepted 31st July 2026

DOI: 10.1039/d6ey00123h

rsc.li/eescatalysis

Broader context

Making chemicals more sustainably requires processes that do not rely on precious catalysts, high temperatures, or centralized infrastructure. Water microdroplets have recently emerged as unique reaction environments, capable of driving spontaneous redox chemistry under ambient, catalyst-free conditions. However, tuning their reactivity, increasing their productivity, and understanding their selectivity are still open frontiers. In this work, we demonstrate how short-chain alcohols can be used as interfacial additives in sonicated emulsive water microdroplets (SEWMs) to enhance their redox reactivity towards producing two key chemicals for industry: hydrogen peroxide as a safe and clean oxidizing agent, and hydrogen as a crucial species for reduction processes. Using SEWMs and our identified conditions, it is possible to generate high concentrations of these and other chemicals in a highly convenient manner. To understand the physical underpinnings of our observations, we used advanced computational simulations to understand how alcohols re-structure the water/oil interfaces, elucidating changes in the bonding of water molecules and how they enhance local electric fields. These findings establish molecular additives such as alcohols as a versatile strategy for restructuring microdroplet interfaces while also establishing alcohol-containing SEWMs as potentially deployable platforms for safe and inexpensive catalyst-free redox chemistry.

[a] *Department of Chemistry, University of Illinois Urbana-Champaign, Urbana, IL 61801, USA. E-mail: joaquinr@illinois.edu*
[b] *Beckman Institute for Advanced Science and Technology, University of Illinois Urbana-Champaign, Urbana, IL 61801, USA*
[c] *Department of Materials and Science Engineering, University of Illinois Urbana-Champaign, Urbana, IL 61801, USA*
[d] *Argonne National Laboratory, Lemont, IL 60439, USA*
† Equal contribution.
‡ Present address: Department of Chemical and Biological Engineering, Princeton University, Princeton, NJ 08544, USA.

1. Introduction

Redox reagents produced from water and air, such as hydrogen (H_2) and hydrogen peroxide (H_2O_2), are a cornerstone for renewability and decarbonization of the chemical industry. H_2O_2 is an attractive oxidant that cleanly decomposes to water

upon reaction.[1,2] It is widely employed across industries, including paper and pulp bleaching, textile processing, electronics production, and chemical manufacturing, where it enables selective oxidative transformations such as propylene to propylene oxide and Baeyer–Villiger oxidation.[1,3–8] Despite this versatility, H_2O_2 is almost exclusively produced by the centralized, large-scale anthraquinone autoxidation process: a multistep, solvent-intensive route requiring large-scale extraction and purification infrastructure.[9–11] As a result, on-site H_2O_2 production is impractical for many applications. In a complementary role, H_2 serves as a reducing agent critical to many significant chemical processes, such as the Haber–Bosch process and a broad class of catalytic hydrogenation reactions.[12–15] Beyond its chemical feedstock role, H_2 is widely regarded as one of the world's most promising clean fuels.[13–15] However, H_2 is predominantly produced *via* the steam methane reformation, an energy-intensive process involving elevated temperatures and pressures.[16,17] While H_2 and H_2O_2 are still traditionally produced *via* thermochemical, large-scale manufacturing processes, there has been widespread interest in alternate methods of production, ranging from electrolysis, electrocatalysis, photocatalysis, and bio-inspired frameworks that seek to enable a more decentralized, modular generation of these chemicals.[15,18,19]

A striking reaction involving the spontaneous production of H_2O_2 and H_2 is that which occurs within aqueous microdroplets.[20–23] Recent work in our group on sonicated emulsive water microdroplets (SEWMs) has shown the intrinsically reductive nature of these systems involving redox between the aqueous and oil phases to generate products in the absence of added catalysts.[23] SEWMs are formed by creating water–hexadecane emulsions *via* sonochemical excitation, displaying H_2 evolution and H_2O_2 formation at mM concentrations, in the latter case primarily originating from the reduction of dissolved O_2.[23] Ultrasonication provides a unique approach to generating reactive microdroplet environments by combining acoustic cavitation with liquid–liquid emulsification. Ultrasonic excitation of liquid systems produces transient cavitation bubbles capable of generating extreme local temperatures and pressures, leading to the formation of reactive radical species including hydroxyl radicals and hydrogen atoms in aqueous-based systems.[24–26] In traditional bulk-phase sonochemical systems, recombination of these species can lead to the formation of H_2O_2 and H_2, respectively, while cavitation-driven chemistry can facilitate reactions occurring at nearby liquid–liquid interfaces.[24–27] Ultrasonication has been widely employed for chemical degradation, interfacial redox-driven nanoparticle synthesis, and oxidative transformations both in microdroplet systems and traditional bulk-phase sonochemical systems.[28–34] However, unlike conventional sonochemical systems, SEWMs introduce an additional biphasic interface that can influence chemical reactivity, alter reactant partitioning and activate reagents at the water/oil interface. Recent studies including our own have expanded the scope of ultrasonically generated biphasic microdroplet systems, demonstrating H_2O_2 formation, hydrocarbon and pollutant degradation, and radical polymerization in water-in-oil microdroplets.[23,35–39] While these studies demonstrate the versatility of ultrasonically generated microdroplets, they have largely focused on establishing new reaction platforms rather than understanding how molecular-level modification of the interface governs chemical reactivity.

Ours and other studies underscore the role of interface-mediated oxygen activation at aqueous microdroplets, and indeed these are emerging as systems providing a large range of chemical transformations under mild, catalyst-free, ambient conditions.[23,40,41] Notably, aqueous microdroplets exhibit enhanced chemical reactivity, enabling reaction accelerations by several orders of magnitude and providing pathways unavailable in bulk-phase water.[42–44] These enhancements are widely attributed to their high interfacial area and the unique properties of the microdroplet interface. For example, strong electric fields probed experimentally and computationally have been implicated in the production of reactive oxygen species such as $OH^{\bullet}$ from water.[20,45–47] Additional interfacial phenomena such as contact electrification, charge accumulation, and enhanced molecular ordering have also been proposed to contribute to microdroplet reactivity, helping modulate charge transfer across water/air and water/oil interfaces.[21,48,49] As a result of their unusual reactivity and flexibility of generation methods, microdroplets have had a rich variety of applications including polymerization, redox transformations, and organic synthesis.[39,50–67]

Existing efforts to tune aqueous microdroplet reactivity have encompassed both external parameters, such as gaseous environment, as well as internal parameters, such as pH and ion modulation.[54,68–71] However, less attention has been devoted to molecular-level restructuring of the microdroplet interface and its effects on reactivity. Prior work has explored how introducing long-chain surfactants into oil–water systems can drastically decrease the charge of microdroplets and reduce overall microdroplet reactivity by disrupting the oil–water interface.[21] But the impact of small, water-miscible amphiphiles that preferentially reside at the droplet interface while not adversely affecting it remains underexplored.

Here, we utilize short-chain alcohols as a class of additives to directly modulate the redox activity of sonicated emulsive water microdroplets (SEWMs) by tailoring the microdroplet interface, extending fundamental insight into microdroplet interfacial chemistry and offering new handles for enhancing redox reactivity and selectivity. Short-chain alcohols have been utilized in the sonolysis-based generation of both H_2O_2 and H_2 from single-phase systems (*i.e.*, aqueous alcohol solutions), by employing intense sonolysis through specialty equipment.[72] In contrast, we have found that using the biphasic system represented by SEWMs offers a much simpler approach, where a low-cost, commercial ultrasonic bath is sufficient to generate H_2 and H_2O_2 in quantities that are not only straightforwardly detectable, but also promising for the on-demand production of these chemicals. Specifically, we show how primary alcohols enhance SEWMs overall production towards H_2O_2 and H_2 under various alcohol concentrations and ultrasonication times. We additionally show how product selectivity can be tailored by modulating the dissolved O_2 content and how

primary alcohols are key to enhancing microdroplet reactivity. We characterize a variety of oil and alcohol oxidation products and discuss the role that the complementary oxidative reaction may play in the kinetic modulation of these systems. Finally, to better understand the role of alcohol in these microdroplet systems, we turn to molecular dynamics (MD) simulations to better understand how alcohols modulate the water–oil interface and tailor overall microdroplet reactivity.

2. Materials and methods

2.1 Chemicals and materials

Methanol (ACS grade, >99.8%) was purchased from Macron Fine Chemicals. Ethanol (200 Proof) was purchased from Decon Labs. 1-Propanol (98.5%), potassium iodide (>99.0%), and hydrogen peroxide (30%, ACS grade) were purchased from Fisher Chemical. Isopropanol (99.5%) was purchased from Honeywell Burdick and Johnson. 1-Butanol (99%) and *tert*-butyl alcohol (99.0%) were purchased from Tokyo Chemical Industry. 2-Butanol (99%) and hexadecane (99%) were purchased from Thermo Scientific. Hydrochloric acid (37%) and soluble starch were purchased from Sigma Aldrich. D_2O and ^{13}C-labeled methanol-d_4 (99%) were purchased from Cambridge Isotope Laboratories. All aqueous solutions were made using type 1 water (18.2 MW cm) obtained from a Milli-Q purification system. Disposable glass scintillation vials were purchased from VWR (#66022-128). Centrifugation was performed using a VWR Galaxy 14D centrifuge. Catalase (bovine liver) was purchased from Alkali Scientific. Phosphate-buffered saline (pH 7.4) was purchased from Corning.

2.2 Preparation of microdroplet emulsions

SEWMs were generated with a Branson CPX1800H ultrasonic water bath with an output power of 70 W and a frequency of 40 kHz. For all samples, a 1 : 10 mixture of aqueous phase to hexadecane oil was prepared by mixing 200 μL of aqueous solution with 2 mL of hexadecane. This mixture was prepared in a 20 mL glass scintillation vial (VWR #66022-128) and ultrasonicated in the bath filled to the operating level marked by the model. All vials were closed with a screw-on septum cap to ensure an airtight seal. Each vial was clamp suspended one inch below the operating level and confined to the center of the water bath using a custom, 3D-printed lid to ensure reproducible and proper ultrasonication (Fig. S1). For gas purged trials, the vial was sealed with one square of parafilm, and a purging needle was placed in the aqueous portion of the mixture to be ultrasonicated. Each gas purged trial was purged for 10 minutes and then promptly sealed with an additional square of parafilm and sealed with a screw-on septum cap. The solution in the ultrasonic water bath was replaced between every trial to ensure the starting water bath temperature was the same.

Mechanical emulsions were investigated through stirring and vortexing. The same aforementioned volumetric ratio and volume was utilized. For stir trials, the mixture was prepared in the same 20 mL glass scintillation vials with a magnetic stir bar, and then stirred for 30 minutes with a IKA C-MAG HS 7 control magnetic hotplate stirrer at 700 rpm. For vortex trials, the mixtures were prepared in VWR centrifuge tubes, sealed with parafilm, and then vortexed with a Thermo Scientific 120 V Digital Vortex Mixer at 2000 rpm for 30 minutes.

2.3 Brightfield microscopy and image analysis of SEWMs

To image microdroplets, solutions were ultrasonicated for 5 minutes, and then immediately transferred to the microscope, whereupon videos and images were captured. Imaging of the microdroplet emulsions was performed in bright-field mode using an inverted epifluorescence microscope (Olympus IX71) equipped with a CMOS camera (Grasshopper 3, FLIR) and a 0.8 numerical aperture (NA) 40× objective lens (Olympus). Videos and images were captured in 1920 × 1200 at 30 Hz. However, for analysis, only 3.75 frames per second were processed using a custom MATLAB script designed to identify and characterize droplets. The workflow begins by adjusting the image intensity and generating a secondary, Gaussian-smoothed image to suppress digitization noise. While this smoothed image is used to detect candidate particles *via* selection of local maxima, the actual sub-pixel localization is performed on the primary image using 2D Gaussian fitting. The algorithm also employs Sobel edge detection and mitigates pixelation effects by extracting particle subregions and centering them using linear interpolation. Finally, the dataset is refined through multiple filtering. Briefly, particles falling outside defined parameter thresholds and particles, whose separation from their nearest neighbors is below a threshold value, were excluded.

2.4 Iodometric detection of H_2O_2

H_2O_2 was detected and quantified *via* a starch-based iodometric assay utilizing a Shimadzu UV-1280 spectrophotometer. 5 μL of H_2O_2-containing aqueous solution was mixed with 1 mL of 0.1 M HCl, 0.2 mL of 1 M KI, 0.2 mL of 0.5% (w/v) starch solution, and 95 μL of type 1 water in a 2 mL quartz glass cuvette. The solution was then stirred by pipetting the mixture out and in two times. The solution changes from transparent to purple, indicating the presence of H_2O_2. The absorption at 572 nm was recorded after 5 minutes of incubation and a spectrum was obtained from 400–800 nm. To detect H_2O_2 in ultrasonicated samples, the aqueous phase was first extracted *via* centrifugation at 10k rpm for 5 minutes, and was then added to the cuvette, following the aforementioned workflow. Centrifugation was performed using a VWR Galaxy 14D centrifuge. All H_2O_2 yields were quantified using a calibration curve generated with this assay (Fig. S2). To ensure accurate quantification of the highest performing SEWMs, oxygen purged SEWMs were diluted 2× prior to analysis to ensure their absorbances lay within the linear calibration range. Additionally, known concentrations of H_2O_2 were spiked into representative mixtures containing all reagents and major products prior to analysis to validate assay performance (Fig. S2). To confirm that the iodometric response originated from H_2O_2, catalase quenching controls were performed. Representative SEWMs samples (50 μL) were incubated with

catalase (10 μL at 10 mg mL^{-1} at pH 7.4) for 10 minutes prior to analysis (Fig. S3 and S4). The iodometric response decreased by 90% following catalase treatment, confirming that H_2O_2 was the dominant contributor to the measured signal.

2.5 Detection of H_2 *via* gas chromatography

Gas chromatography (GC) analysis was conducted using a Thermo Fisher TRACE 1600 GC instrument equipped with a TRACE 1610 permanent gas analyzer outfitted with two thermal conductivity detectors (TCD). Two packed columns (Thermo Fisher, 26017900, 5 Å molecular sieve (MS-5A), and a Thermo Fisher, 26017800, porous polymer network (PP-N)) were employed for the separation, following the plumbing scheme denoted in Fig. S5. The inlet temperature and oven were maintained at 80 °C. Both TCD detectors and filaments were set to 200 °C and 300 °C, respectively. The L-TCD and R-TCD were set to positive and negative polarities, respectively. Both detectors had a reference flow of 1 mL min^{-1}. The L-TCD utilized He while the R-TCD utilized N_2 as carrier gases.

Gaseous samples were manually injected into the permanent gas analyzer, where the first channel (Aux L-TCD) serves for the separation and detection of CO_2, O_2, N_2, CH_4, and CO with He as the carrier. The second channel (Aux R-TCD) serves for the separation and detection of H_2 with N_2 as the carrier. For H_2, CO_2, CH_4, and CO detection from sonicated samples, 5 mL of gaseous samples were extracted from the trapped headspace of the sealed vials immediately following sonication and subsequently injected into the TRACE 1600 GC using a Hamilton gastight syringe (PN: 81520). All H_2, CO_2, CH_4, and CO yields were quantified using their respective calibration curves and normalized by injection volume to calculate the concentration of evolved gaseous species (Fig. S6–S9). Known standards of H_2 (Ar/H_2, 97/3%) and CO_2 (99.999%) were purchased from SJ Smith. CH_4 (99.9%) and CO (99%) were purchased from Sigma-Aldrich.

2.6 Detection of oxidation products *via* NMR

All NMR measurements were conducted on a Bruker NEO 600 MHz NMR spectrometer, equipped with a 5 mm BBO prodigy probe. For analysis of products in the distinct phases after forming SEWMs, 500 μL of the aqueous phase was diluted in 100 μL of D_2O in NMR tubes for ^1H and ^{13}C NMR spectra. ^1H NMR spectra for the aqueous phase were acquired with 256 scans, and ^{13}C NMR spectra were acquired with 4096 scans. For quantitative NMR (qNMR), 48.5 mM triphenylphosphate (TPP) in $CDCl_3$ was used as the external calibration compound. To confirm spectral assignments, the aqueous extract was spiked with known standards (10 mM each of acetic and formic acid, 4 mM each of ethanol and methanol), and ^1H NMR spectra were recorded before and after spiking with 256 scans. All aqueous ^1H NMR spectra were obtained using a water suppression pulse sequence to enhance the signal to noise ratio.

2.7 Simulations of the water–oil microdroplet interface

2.7.1 System preparation. In each system for molecular dynamics simulations, 3500 water molecules were simulated to form a 3 nm droplet. Each system contains 2800 hexadecane molecules to achieve a water : oil ratio of 1 : 10. Seven different alcohol–water/oil systems were constructed: methanol (MeOH), ethanol (EtOH), 1-propanol (PrOH), 1-butanol (BuOH), 2-butanol (2-BuOH), isobutanol (i-BuOH), and *tert*-butanol (*t*-BuOH), as well as an alcohol-free system used as a control model. For MeOH, three concentrations were simulated (100 mM, 500 mM, and 1000 mM), using 7, 35, and 70 MeOH molecules, respectively. For the other alcohol systems, 35 molecules were added to achieve ~500 mM concentration.

2.7.2 Molecular dynamics simulations. Molecular dynamics simulations were performed with GROMACS 2024.6[73] package with OPLS-AA force field[74,75] and TIP4P water. Partial atomic charges for the alcohol molecules were derived from *ab initio* electrostatic potential fitting using the CHelpG scheme, as implemented in Gaussian 16.[76] An initial energy minimization was performed to obtain the ground-state structure. The Nose–Hoover thermostat was used to stabilize the system temperature at 300 K with a time constant of 1 ps and the Parrinello–Rahman barostat was used to maintain the pressure at 1 bar with a time constant of 10 ps (NPT). Three-dimensional periodic boundary condition (PBC) was applied, and a spherical cut-off of 1.4 nm was used for all van der Waals (vdW) interactions. The particle-mesh Ewald (PME) with 1.4 nm cutoff for long-range electrostatic interactions were used throughout the simulations. Each system was simulated for 20 ns under the NPT conditions for production run with a 2 fs timestep. The last 10 ns simulation data were used for analysis with MDAnalysis package[77] and in-house python scripts (provided in Note S1).

2.7.3 Hydrogen bonding analysis. The number of water–water hydrogen bonds was calculated using the gmx hbond-legacy utility in GROMACS, employing a donor–acceptor distance cutoff of 0.35 nm and a hydrogen–donor–acceptor angle cutoff of 30°. For alcohol-containing systems, water molecules were classified into near and far groups relative to alcohol oxygen atoms with a cutoff of 0.5 nm, while in alcohol-free droplets, interfacial waters were defined by proximity to oil heavy atoms with a cutoff of 0.5 nm. Index groups for near, far, or interfacial waters were generated from the trajectories, and hydrogen bond lifetimes were averaged over 10 anchor frames from the last 1000 trajectory frames.

The H-bond lifetime was quantified from the time autocorrelation function of H-bond existence, $C(t)$:

$$C(t) = \frac{\langle h(0)h(t)\rangle}{\left\langle h(0)^2\right\rangle}$$

where $h(t)$ = 1 if a given donor–acceptor pair is H-bonded at time t, and 0 otherwise.

Two types of lifetimes were computed: (1) continuous lifetime, where bond must persist without interruption and (2) intermittent lifetime, where bond may break and reform. The effective lifetime τ was then obtained by integrating the correlation function:

$$\tau = \int_0^\infty C(t)\mathrm{d}t$$

where $C(t)$ is the hydrogen-bond autocorrelation function evaluated at time t.

2.7.4 Hexadecane orientational order parameter. To quantify the structural response of the oil phase adjacent to the microdroplet interface, we computed an orientational order parameter (S) for interfacial hexadecane molecules. Hexadecane was chosen as a representative long-chain hydrocarbon to probe ordering and alignment effects induced by the presence of the aqueous microdroplet and interfacial alcohols. Hexadecane molecules were first identified at the droplet interface based on proximity to interfacial water molecules. A hexadecane molecule was classified as interfacial if any of its heavy atoms lay within a cutoff distance R_{iface} of interfacial water oxygen atoms. The cutoff distance was chosen to capture molecules in direct contact with the water–oil boundary while excluding bulk oil molecules.

For each selected hexadecane molecule, a molecular orientation vector u was defined along the principal molecular axis, taken as the normalized vector connecting the terminal carbon atoms of the alkyl chain. The orientational order parameter S then was calculated relative to the local surface normal of the droplet, defined as the outward radial vector from the droplet center of mass to the molecular center of the hexadecane chain. The order parameter was computed as:

$$S = \frac{1}{2}\left(3\left\langle \cos^2\theta \right\rangle - 1\right)$$

where θ is the angle between the hexadecane molecular axis u and the surface normal, and $\langle \cdots \rangle$ denotes averaging over all interfacial hexadecane molecules and over the analyzed trajectory frames.

Values of $S = 1$ correspond to perfect alignment of hexadecane chains normal to the droplet surface, and $S = 0$ indicates isotropic orientational disorder. Time-resolved and ensemble-averaged order parameters were evaluated over the last 10 ns of the simulations for alcohol-containing and alcohol-free systems, as well as between hexadecane molecules in direct contact with alcohol molecules and those further away from the alcohol. An in-house python code (Note S1) was used to evaluate the hexadecane order parameter in the water–oil systems.

2.7.5 Water dipole orientation. For each water molecule, the dipole vector ($\vec{\mu}$) was defined from the oxygen atom (OW) to the midpoint of the two hydrogens (HW1, HW2). The local surface normal $\hat{r}$ was taken as the radial vector pointing from the droplet center-of-mass (COM) to the oxygen position.

The orientational order parameter was computed as:

$$\cos\theta = \frac{\vec{\mu}\cdot\hat{r}}{\|\vec{\mu}\|\|\hat{r}\|}$$

where θ is the angle between the dipole moment and the radial direction. Histograms of $\cos\theta$ and time-averaged values were used to assess whether dipoles preferentially point inward ($\cos\theta < 0$) or outward ($\cos\{\theta\} > 0$) at the droplet interface. Distributions of $\cos\theta$ were constructed over the last 5 ns of the trajectories to characterize dipole alignment relative to the droplet interface. An in-house python code (Note S1) was used to process the MD simulation trajectory for dipole orientation calculations.

2.7.6 Electric field calculations. To quantify local electric fields acting on water, additional rerun simulations were performed with Coulomb-only forces. For the TIP4P model, forces on the virtual charge site (MW) were assigned to the corresponding oxygen. The instantaneous electric field vector, $\vec{E}$, at each interfacial water oxygen was obtained as:

$$\vec{E} = \vec{F}/q$$

where $\vec{F}$ is the force vector on the oxygen atom and q is the effective charge of the TIP4P virtual site. The field was projected along the local normal to obtain a scalar measure of the field:

$$E_{\text{normal}} = \vec{E}\cdot\hat{r}$$

Near *vs.* far waters were classified based on their distance to alcohol oxygen atoms within a cutoff of 0.5 nm. Mean and standard deviation of E_{normal} were computed over the last 5 ns of trajectories. An in-house python code (Note S1) was used to evaluate the electric field on the interfacial water molecules.

3. Results and discussion

3.1 Confirmation of SEWMs formation and reactivity towards H_2O_2 and H_2 production

First, we validated the generation of water microdroplets under ultrasonication in the presence and absence of alcohol, specifically looking at mixtures of 500 mM methanol, ethanol, or 1-propanol containing SEWMs in addition to alcohol-free SEWMs. SEWMs were generated by mixing 1 to 10 volumetric ratios of aqueous solution to hexadecane. To validate microdroplet formation under ultrasonication, bright-field microscopy was used to characterize the average microdroplet diameters (Fig. 1A). Alcohol-free SEWMs exhibited similar size distributions compared to methanol-containing SEWMs with average diameters of 3.0 ± 0.9 μm and 3.1 ± 1.4 μm, respectively (Fig. 1B and C). These results suggest that methanol does not significantly alter the microdroplet size under these ultrasonication conditions. In contrast, methanol-containing SEWMs generated about 2× more detectable microdroplets over the same observation period. This suggests a difference in microdroplet formation ability and stability within the two different biphasic systems. Notably, the number of water and methanol-containing SEWMs drastically decreased over time, indicating that the SEWMs were gradually coalescing to form a single phase. Note that the total droplet counts in Fig. 1B and C represent the cumulative sum of detections across all frames and do not distinguish unique droplets between consecutive frames. Interestingly, methanol-containing SEWMs were distinct amongst all alcohol-containing SEWMs, generating significantly more microdroplets and producing the smallest microdroplet diameter sizes out of any of the alcohol-containing SEWMs (Fig. S10–S12). In comparison to alcohol-free SEWMs, ethanol and 1-propanol containing SEWMs generated fewer and larger microdroplets on

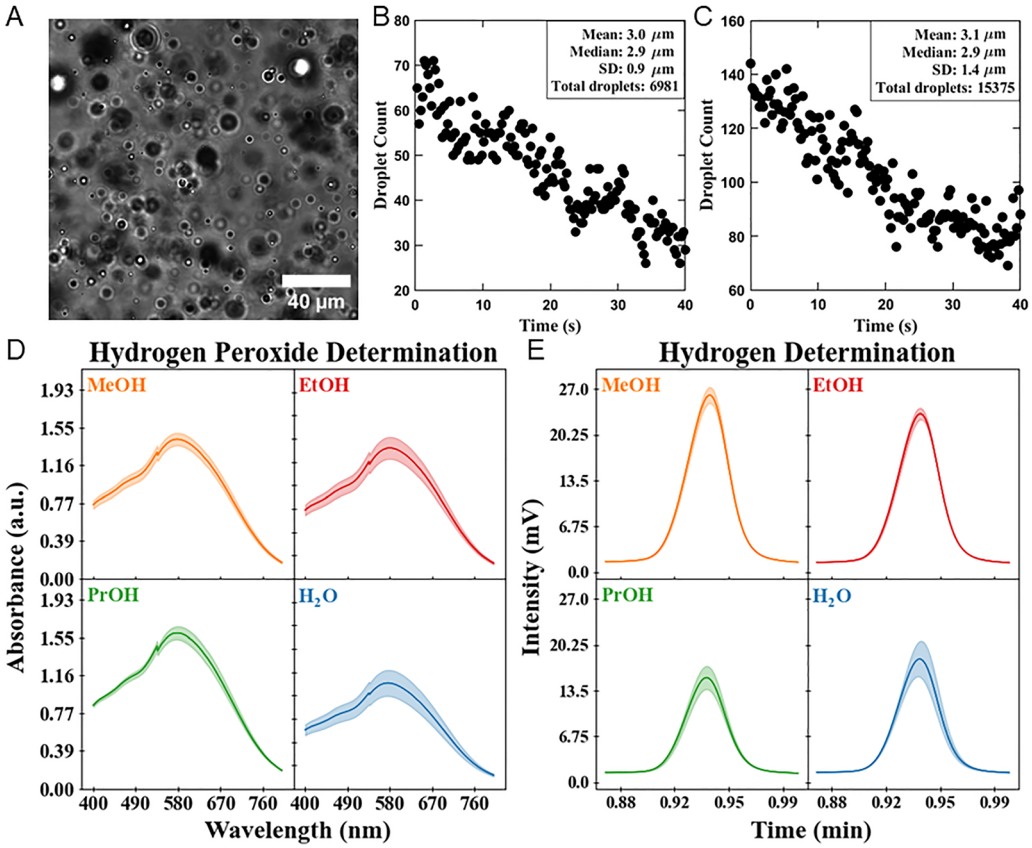

Fig. 1 Confirmation of SEWM formation and reactivity towards H_2O_2 and H_2 generation. (A) Brightfield image (40× magnification) showing the formation of water SEWMs after 5 minutes of ultrasonication. (B) Temporal evolution of detected droplets in each individual frame is plotted against time (seconds). The legend displays the mean, median, and standard deviation (SD) of the droplet count across the duration of the recording of alcohol-free SEWMs and (C) methanol (MeOH)-containing SEWMs. (D) UV-Vis spectra of the starch iodine system in the presence of the aqueous phase of SEWMs, indicating H_2O_2 detection, after 30 min of ultrasonication; average of data shown in triplicate with shaded region indicating one standard deviation for n = 3. (E) Gas chromatograms of the trapped headspace in SEWMs containers, showing the generation of hydrogen. All alcohol-containing SEWMs had an initial concentration of 500 mM; average of data shown in triplicate with shaded region indicating one standard deviation for n = 3.

average. These results suggest that alcohol identity may play a key role in influencing droplet formation and affect the dynamic population of SEWMs during ultrasonication.

After validating microdroplet formation, we probed the reactivity towards H_2O_2 and H_2 generation on 500 mM alcohol-containing SEWMs. Ultrasonication was applied for 30 minutes and the yields for these products were analyzed. H_2O_2 detection was carried out colorimetrically *via* a starch-based iodometric assay resulting in the UV-vis spectra as seen in Fig. 1D. Quantification was performed using a calibration curve generated *via* the assay (Fig. S2). To confirm that the iodometric signal originated from H_2O_2, catalase-quenching controls were performed on representative SEWMs samples, reducing the iodometric response by 90% (Fig. S3 and S4). Using this validated assay, 500 mM methanol, ethanol, and 1-propanol containing SEWMs all produced significantly greater H_2O_2 quantities than alcohol-free SEWMs after 30 minutes of ultrasonication, generating 23 ± 1 mM, 22 ± 2 mM, and 26 ± 1 mM H_2O_2, respectively. Comparatively, alcohol-free SEWMs only produced 17 ± 2 mM H_2O_2 after 30 minutes of ultrasonication (Fig. S13). For the same trials, H_2 generation in the headspace was quantified using gas chromatography (GC). As seen in Fig. 1E, alcohol-containing SEWMs also increased the amount of H_2 produced, with methanol, ethanol, and 1-propanol containing SEWMs generating 387 ± 20 μM, 342 ± 17 μM, and 219 ± 28 μM H_2, respectively, *versus* alcohol-free SEWMs generating 264 ± 46 μM H_2 after 30 minutes of ultrasonication (Fig. S14). Notably, only methanol- and ethanol-containing SEWMs yielded a drastic increase in both redox probes. 1-Propanol containing SEWMs featured a difference in redox probe selectivity, preferentially generating more H_2O_2 and less H_2 in comparison to alcohol-free SEWMs. Interestingly, enhanced redox activity did not correlate strictly with smaller microdroplet sizes as has been suggested previously for microdroplets at the water–air interface.[42] Ethanol-containing SEWMs produced fewer and larger microdroplets than alcohol-free SEWMs, yet still exhibited increased yields of both redox products, suggesting that droplet size alone does not govern redox activity. Instead, the alcohol-dependent changes in microdroplet population and their interfacial properties likely contribute to the enhanced redox behavior observed in SEWMs. For methanol-containing SEWMs, the increased number of

microdroplets may contribute to their observed enhanced reactivity by increasing the overall interfacial area. Collectively, these results demonstrate that short-chain alcohols enhance the redox activity of SEWMs. As an additional control, single-phase aqueous systems ultrasonicated for 30 minutes in the absence of oil (Fig. S15) led to the generation of minor amounts of H_2 and H_2O_2, at 100× less quantity than SEWMs, indicating the essential role of the biphasic system in driving this redox activity. To further distinguish SEWM-associated redox activity from bulk sonochemical processes, additional control experiments were performed using varied ultrasonication conditions and alternative mechanical mixing methods. Reducing the ultrasonication power from 100% to 70% resulted in comparable H_2 and H_2O_2 production trends (Fig. S16 and S17), suggesting that the observed enhancement is not solely dependent on the applied ultrasonication power. Additionally, we performed stirring and vortexing experiments to evaluate whether simple mechanical mixing could generate comparable redox activity. However, neither method produced observable microdroplet formation or detectable quantities of H_2 and H_2O_2 (Fig. S16 and S17), demonstrating the necessity of ultrasonication to generate redox-active SEWMs.

3.2 Effects of ultrasonication time and alcohol concentration on H_2O_2 and H_2 production

To further understand the role alcohol plays in this system, we investigated the time-dependent formation of H_2O_2 and H_2 for 500 mM-containing alcohol SEWMs across 10-, 20-, and 30-minute ultrasonication time windows (Fig. 2 and S18). At the shorter ultrasonication time of 10 minutes, there is no significant difference in the yield of the redox probes between alcohol-containing and alcohol-free SEWMs. However, when ultrasonicated for 30 minutes, alcohol-containing SEWMs consistently outperform alcohol-free SEWMs in H_2O_2 and H_2 generation. From the time-dependent trials, product generation rates were able to be approximated (Fig. S19 and S20). Alcohol-free SEWMs produced 0.41 mM min^{-1} H_2O_2 and 8.1 μM min^{-1} H_2. In contrast, alcohol-containing SEWMs displayed much higher rates of production with different product selectivity depending on alcohol identity: methanol produced H_2 the fastest (H_2O_2 at 0.72 mM min^{-1} H_2O_2 and H_2 at 13 μM min^{-1} H_2), ethanol increased the formation rate of both probes (0.66 mM min^{-1} H_2O_2 and 12 μM min^{-1} H_2), and 1-propanol increased H_2O_2 generation but decreased the rate of H_2 generation (0.83 mM min^{-1} H_2O_2 and 6.6 μM min^{-1} H_2). In previous work, we had reported that interrupting ultrasonication led to a sudden decrease in the production of H_2.[23] Thus, we performed additional post-sonication control experiments where we monitored species production after interrupting and resting the samples. These experiments revealed that H_2O_2 concentrations continued to increase slightly (~15%) after ultrasonication ceased, whereas H_2 concentrations remained unchanged, indicating that continuous ultrasonication is required for continued H_2 formation but not for continued H_2O_2 production (Fig. S21 and S22). These results are consistent with what has been reported on microdroplets, implicating a contribution from the evolution of the water/oil interface within the microdroplet in addition to ultrasonically induced cavitation.[23,36–38] Notably, the degree of enhancement after sonication ceased was dependent upon the SEWMs composition. Alcohol-containing SEWMs generated a greater amount of H_2O_2 in comparison to alcohol-free SEWMs when allowed to age for equal times. These observations suggest that alcohols modify the redox chemistry of SEWMs even after ultrasonication has ceased, allowing continued enhanced peroxide formation.

We also systematically investigated the effect of initial alcohol concentration on the redox activity of the SEWMs. The initial alcohol concentration was varied (100 mM, 500 mM, and 1 M) across 30-minute ultrasonication times, and the resulting H_2O_2 and H_2 yields were quantified (Fig. 3 and S23). For methanol- and ethanol-containing SEWMs, high initial concentrations outperformed lower concentrations with 1 M trials producing 29 ± 1 and 26 ± 1 mM H_2O_2, respectively, whereas the corresponding 100 mM trials produced only 23 ± 1 and 22 ± 2 mM H_2O_2. In contrast, 1-propanol containing SEWMs exhibited higher H_2O_2 yields with lower initial alcohol concentrations. Specifically, 100 mM propanol trials produced 26 ± 2 mM H_2O_2, whereas the corresponding 1 M trials

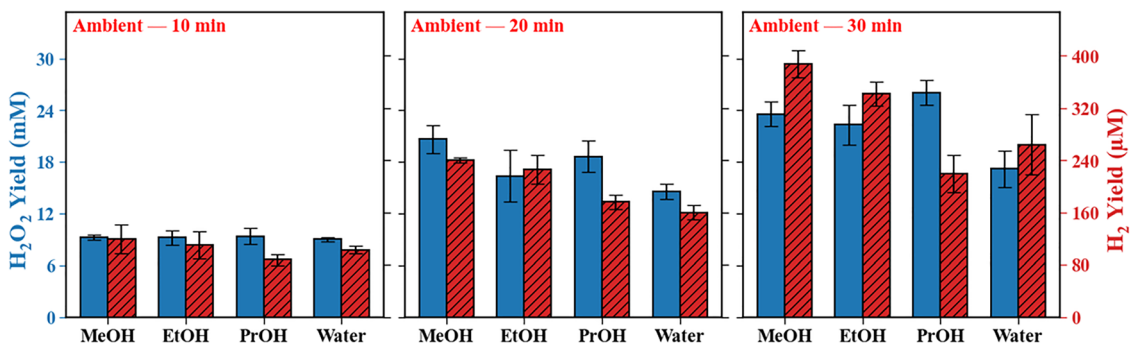

Fig. 2 The sonication time dependence of SEWMs reactivity. Hydrogen peroxide (blue) and hydrogen (red) yields from aqueous microdroplets containing methanol, ethanol, and 1-propanol at a concentration of 500 mM compared to water. Microdroplets were ultrasonicated under ambient atmosphere for 10, 20, and 30 minutes. Alcohol-containing microdroplets consistently enhance H_2O_2 production under increasing ultrasonication times relative to water and boost H_2 yields for methanol- and ethanol-containing SEWMs.

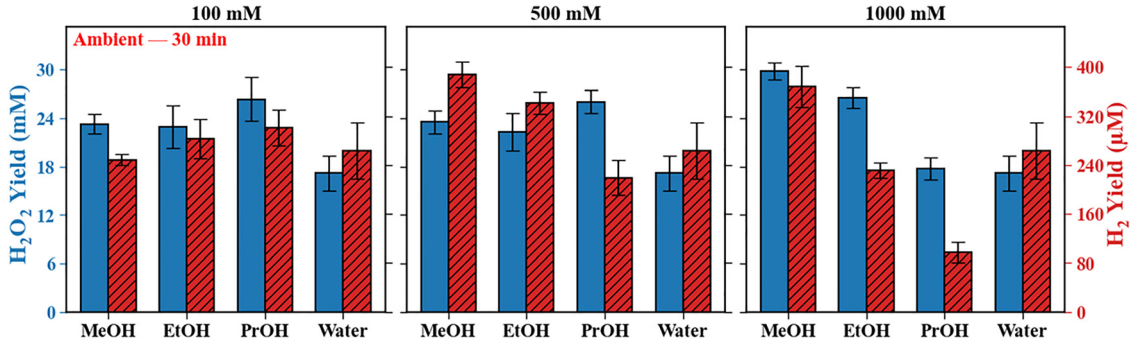

Fig. 3 The alcohol concentration dependence of SEWM reactivity. Hydrogen peroxide (blue) and hydrogen (red) yields from aqueous microdroplets containing methanol, ethanol, and 1-propanol at concentrations of 100 mM, 500 mM, and 1 M compared to water. Microdroplets were ultrasonicated under ambient atmosphere for 30 minutes. Alcohol-containing microdroplets consistently enhance H_2O_2 production and boost H_2 yields at optimal concentrations.

produced only 17 ± 1 mM H_2O_2. These overall trends are mirrored in H_2 generation (Fig. 3), where the shorter carbon chain alcohols performed better at higher initial concentrations whereas the longer chain alcohols performed better at lower initial concentrations. Overall, 500 mM was a consistently high-performing concentration of the three initial alcohol concentrations tested, with these SEWMs generating significantly greater amounts of H_2O_2 and H_2 *versus* alcohol-free SEWMs.

3.3 Tuning H_2O_2 and H_2 product selectivity by modifying the gaseous environment

Prior work in our lab and in other groups has established that ambient and dissolved oxygen serve as a major source of the H_2O_2 formed in aqueous microdroplets *via* its (redox) reduction.[23,40,41] Accordingly, the selectivity of the redox product can be tuned by modifying the local gaseous environment during microdroplet formation. To determine whether alcohol-containing SEWMs also enable tunable selectivity, we conducted experiments under oxygen or argon gas purged conditions, to preferentially promote H_2O_2 or H_2 formation, respectively (Fig. S24). As seen in Fig. 4, purging oxygen leads to the enhanced production of H_2O_2. After 30 minutes of ultrasonication, alcohol-free SEWMs generated 32 ± 1 mM H_2O_2 under O_2 purge *versus* 17 ± 2 mM H_2O_2 under ambient gas atmosphere. This enhancement is even more pronounced for 500 mM alcohol-containing SEWMs. Under oxygen purge, methanol, ethanol, and propanol systems respectively produced 56 ± 7, 42 ± 9, and 39 ± 4 mM H_2O_2 compared to 23 ± 1, 22 ± 2, and 26 ± 1 mM H_2O_2 under ambient gas conditions. For the highest performer, methanol, this represented a ∼2× increase in H_2O_2 yield. For the oxygen purged, alcohol-containing SEWMs, a 2× dilution was performed prior to analysis to ensure accurate H_2O_2 quantification.

In a similar manner, purging argon in enhances H_2 production while limiting H_2O_2 production. Under ambient conditions, alcohol-free SEWMs and 500 mM methanol, ethanol, and 1-propanol containing SEWMs each produced 264 ± 46, 387 ± 20, 342 ± 17, and 219 ± 28 μM H_2, respectively. When argon was purged, they then respectively generated 758 ± 15, 956 ± 27, 887 ± 35, and 670 ± 80 μM H_2, increasing their production up to 3× compared to ambient gas conditions. Importantly, alcohol-containing SEWMs can outperform alcohol-free SEWMs under every purge condition, indicating that microdroplet composition enhances overall reactivity while enabling tuning of redox selectivity *via* selection of the gaseous environment.

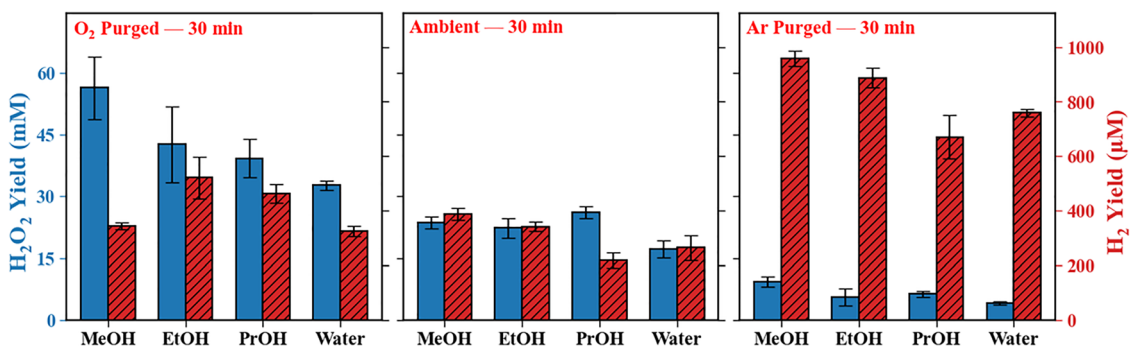

Fig. 4 The effects of environmental gas conditions on SEWM product selectivity (H_2 *vs.* H_2O_2). Hydrogen peroxide (blue) and hydrogen (red) yields from aqueous microdroplets (n = 3) containing methanol, ethanol, and 1-propanol at concentrations of 100 mM, 500 mM, and 1 M compared to water. Vials were purged with oxygen or argon for 10 minutes prior to ultrasonication and then sealed for 30 minutes of ultrasonication. Oxygen purging enhances H_2O_2 yields relative to ambient conditions, whereas argon purging dramatically enhances H_2 generation while lowering H_2O_2 formation.

3.4 The role of the alcohol structure in enhancing redox product yield

To better understand the role of the structure of the alcohols in microdroplet reactivity, we formed SEWMs containing secondary and tertiary alcohols. Herein we ultrasonicated a 1 : 10 mixture of 500 mM 1-propanol, 2-propanol, 1-butanol, 2-butanol, and *tert*-butyl alcohol to hexadecane and examined the amount of H_2O_2 and H_2 produced. The primary alcohols consistently produced more H_2O_2 whereas the branched isomers show suppressed product yields, generating similar amounts to alcohol-free SEWMs (Fig. 5A). As seen, both primary alcohols (1-propanol and 1-butanol) outperform their substituted isomers with regards to H_2O_2 production. 1-Propanol containing SEWMs produce 26 ± 1 mM H_2O_2 *versus* 2-propanol's production of 20 ± 4 mM H_2O_2. Likewise, 1-butanol also outperforms its isomers, producing 20 ± 2 mM H_2O_2 *versus* 2-butanol and *tert*-butyl alcohols' production of 19 ± 1 and 13.6 ± 0.8 mM H_2O_2. Likewise, similar trends emerge regarding H_2 production (Fig. 5B and Fig. S25). Additionally, a clear alcohol chain length dependence emerges overall, with longer alcohol-containing SEWMs featuring a significant decrease in their redox probe production in comparison to shorter alcohols such as methanol and ethanol. A possible explanation is that the microdroplet interface is more poorly structured in the presence of longer, bulkier alcohols with their inherently weaker hydrogen bonding, leading to a decrease in reactivity compared to their primary counterparts. We explore the role of hydrogen bonding in Section 3.6.

3.5 On the redox balance of alcohol-containing SEWMs

Notably, this study has so far focused on the production of H_2O_2 and H_2. While we understand that H_2O_2 primarily arises from the oxygen reduction reaction occuring at the water–oil interface,[23] less is understood about the oxidation reactions that must be taking place to redox balance this system. Prior work in our lab has shown that when hexadecane is reused as the oil component, the oxidation of hexadecane to hexadecanol can be detected *via* ^{1}H NMR, and thus, the reduction of oxygen is balanced by the oxidation of hexadecane.[23] These prior observations suggest that the oxidation of hexadecane can also be occuring to redox balance these alcohol-containing SEWMs. However, in alcohol-containing SEWMs, additional oxidation pathways may become available. To further probe these processes, we characterized the various products that evolve during the continuous generation of alcohol-containing SEWMs. Specifically, we characterized the gaseous and aqueous products that were generated by alcohol-containing and alcohol-free SEWMs under O_2, ambient, or Ar gaseous environments after 30 minutes of ultrasonication utilizing GC-TCD, ^{1}H NMR, ^{13}C NMR, and quantitative NMR (qNMR).

GC analysis revealed that ultrasonication of 500 mM methanol-containing SEWMs under ambient atmosphere produces small molecule carbon-containing gaseous products, evolving 0.12 mM CO_2, 0.17 mM CH_4, and 0.85 mM CO in addition to enhancing H_2 production relative to alcohol-free SEWMs (Fig. 6A). Gaseous product identity was confirmed and quantified by injecting known standards of CO_2, CO, and CH_4 (Fig. S6–S9). Notably, the product distribution of these permanent gases can also be tuned by modulating the dissolved oxygen content of the SEWMs environment, analogous to the redox tuning observed for H_2 and H_2O_2. By analyzing the chromatogram's peak areas corresponding to CO_2, CH_4, and CO, quantitative yields were calculated. H_2 is also included throughout Fig. 6 as a reference to the previously discussed H_2 results.

When methanol-containing SEWMs were ultrasonicated for 30 minutes following O_2 purging, significantly greater amounts of oxygenated gaseous products were observed (Fig. 6B), generating approximately 4.8× more CO_2 (0.64 mM) and 3.4× more CO (1.35 mM) relative to ambient atmosphere conditions. Additionally, the yield of hydrogenated gaseous products decreased for oxygen-loaded *versus* ambient atmosphere conditions,

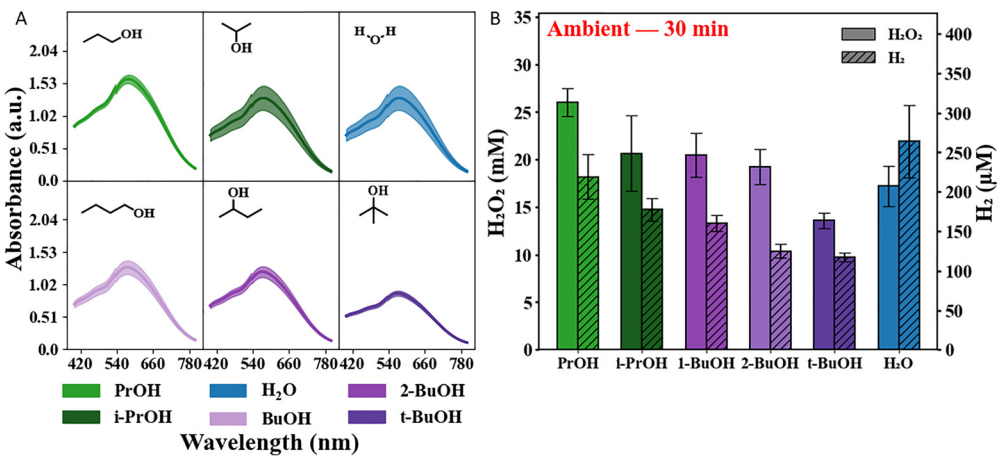

Fig. 5 The alcohol structure dependence on enhancing SEWM reactivity. Primary alcohols are key to enhancing reactivity. (A) The UV-vis response of 30 minute ultrasonicated samples containing 500 mM of 1-propanol, 2-propanol, 1-butanol, 2-butanol, and *tert*-butyl alcohol *versus* water, showing a clear substitution dependence for enhancing H_2O_2 yields. (B) Corresponding H_2O_2 (solid) and H_2 (hashed) yields for each system. A strong trend is observed in which primary alcohols significantly enhance H_2O_2 production, while more substituted alcohols approach yields comparable to alcohol-free SEWMs.

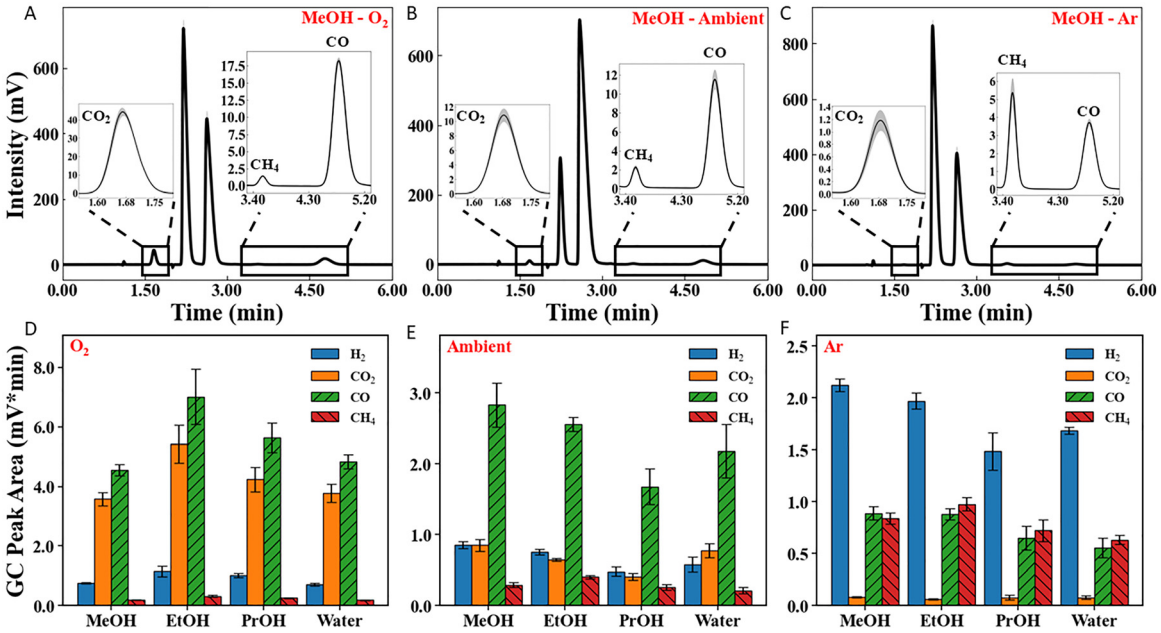

Fig. 6 The GC-TCD analysis of headspace products from SEWMs after 30 minutes of ultrasonication. Samples were purged prior to ultrasonication with (A) O_2, (B) ambient atmosphere, and (C) Ar. In addition to H_2, CO_2, CH_4 and CO are evolved. The selectivity of these products can be tuned by tailoring the gaseous environment of the SEWMs. More oxygenated products such as CO_2 and CO are produced when SEWMs are formed in the presence of O_2 while more hydrogenation products such as H_2 and CH_4 are formed when O_2 is removed from the system. In (D)–(F), the qualitative yield for every gaseous product is shown for 500 mM methanol, ethanol, and 1-propanol containing SEWMs in comparison to pure water SEWMs under the same purge condiitons of (D) O_2, (E) ambient atmosphere, (F) Ar.

generating 0.11 mM *vs.* 0.17 mM CH_4, respectively. Similar to tuning for H_2 yield, ultrasonication of the same system following argon purging resulted in a significant decrease in the yield of oxygenated products and a substantial increase in the production of CH_4 (Fig. 6C). Methanol-containing SEWMs generated trace amounts of CO_2, 66% less CO (0.29 mM), and approximately 4× more CH_4 (0.49 mM) relative to ambient atmosphere conditions, showing the capacity of SEWMs systems to generate hydrogenated products under favorable gaseous conditions. These results suggest a concurrent pathway for the enhanced generation of products *via* reductive pathways, such as H_2O_2 bolstered on an increased oxidation activity reflected in the generation of CO and CO_2.

In addition to analyzing the permanent gases evolved for 500 mM methanol-containing SEWMs, we systematically studied the gaseous product distribution of 500 mM ethanol- and 1-propanol-containing SEWMs, as well as alcohol-free SEWMs under O_2, ambient, or argon gaseous environments after 30 minutes of ultrasonication. The full chromatograms and product peaks are provided in the SI (Fig. S26 and S27). Across all SEWM conditions, similar products were observed and their quantified yields are provided in Table S1. Alcohol addition enhanced the production of CO_2, CO, and CH_4 relative to alcohol-free SEWMs, although the degree of enhancement depended on both alcohol identity and dissolved gas composition. For example, under O_2, ethanol-containing SEWMs produced the most products compared to alcohol-free SEWMs, whereas under ambient and Ar conditions, methanol-containing SEWMs produced the highest yields (Fig. 6D–F). In general, a large increase in the amount of oxygenated products (CO_2 and CO) was observed for all SEWMs systems under O_2 (Fig. 6E), and a significant decrease in oxygenated products was seen with all Ar purged SEWMs systems (Fig. 6F).

As an additional control, we ultrasonicated single-phase hexadecane in the absence of aqueous phase, as it has been shown before that this process evolves carbon products.[78] After 30 minutes of ultrasonication, almost identical amounts of CO_2, CO, and CH_4 were evolved from the ultrasonication of hexadecane compared to alcohol-free SEWMs as detected by GC-TCD analysis (CO_2: 0.11 *vs.* 0.11 mM, CO: 0.62 *vs.* 0.67 mM, CH_4: 0.08 *vs.* 0.12 mM; Fig. S28), indicating that hexadecane oxidation contributes significantly to the observed gaseous carbon product formation. However, the inclusion of alcohols enhanced carbon product yields beyond this baseline, suggesting that the presence of alcohols introduces additional oxidation pathways and further highlights the ability of SEWMs to function as tunable redox microenvironments.

In order to further investigate the role of oil and alcohol oxidation in these systems, we characterized the ability of SEWMs to induce the oxidation of both hexadecane and short-chain alcohols to generate water-soluble, potentially value-added products. We performed NMR measurements on the aqueous phase obtained after ultrasonicating a 1 : 10 water : hexadecane mixture for 30 minutes under ambient conditions. Results from ^{1}H NMR analysis showed the appearance of numerous new signals (Fig. 7A). Upon structural analysis based on the chemical shift values, integrations, and the splitting pattern of each NMR peak, we identified several oxidation

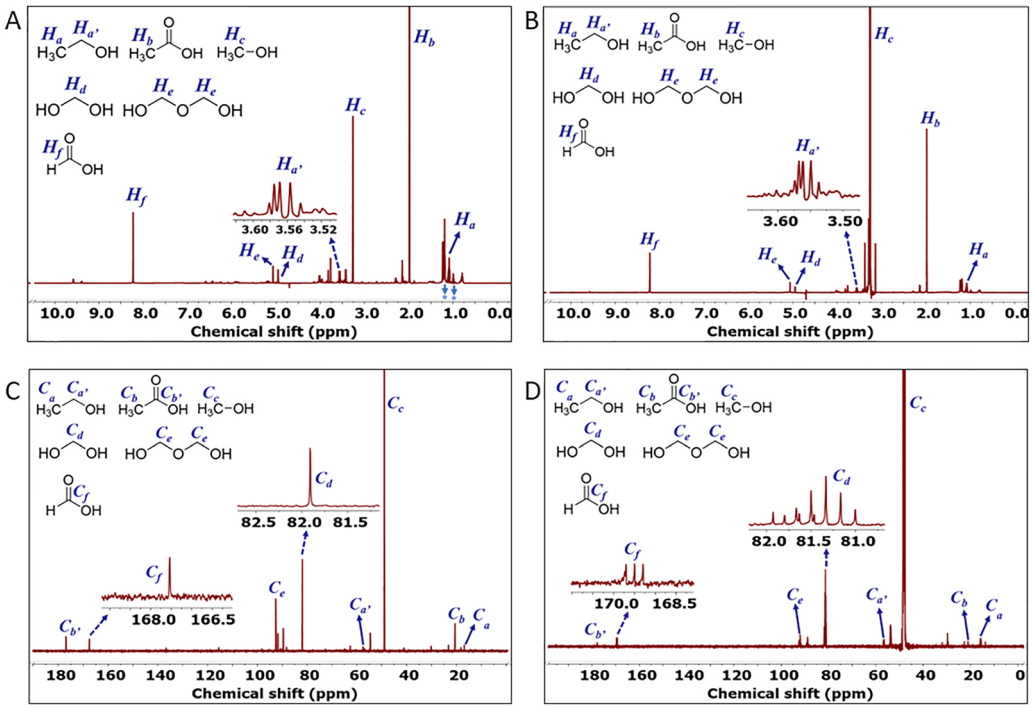

Fig. 7 The NMR data identifying the various oxidation products in SEWMs systems after 30 minutes of ultrasonication. (A) The ^{1}H NMR (600 MHz, H_2O/D_2O) δ 1.08 (t, J = 7.22 Hz, 3H, H_a), 1.98 (s, 3H, H_b), 3.27 (s, 3H, H_c), 3.56 (q, J = 7.18 Hz, 2H, $H_{a'}$), 4.95 (s, 4H, H_d), 5.07 (s, 4H, H_e), 8.23 (s, 1H, H_f) on the aqueous phase of alcohol-free SEWMs. * represents residual hexadecane signals. (B) ^{1}H NMR (600 MHz, H_2O/D_2O) δ 1.08 (t, J = 7.22 Hz, 3H, H_a), 1.98 (s, 3H, H_b), 3.26 (s, 3H, H_c), 3.55 (q, J = 7.18 Hz, 2H, $H_{a'}$), 4.95 (s, 4H, H_d), 5.06 (s, 4H, H_e), 8.22 (s, 1H, H_f) on the aqueous phase of 500 mM methanol-containing SEWMs reveals similar ^{1}H NMR signals. Hydroxy protons corresponding to carboxylic acids, alcohols, and hydrogen peroxide are not detectable due to fast proton exchange and the use of a water suppression pulse sequence. (C) The ^{13}C NMR (151 MHz, H_2O/D_2O) δ 17.12 (C_a), 20.85 (C_b), 49.25 (C_c), 57.8 ($C_{a'}$), 82.18 (C_d), 92.9 (C_e), 167.81 (C_f), 177.24 ($C_{b'}$) on the aqueous phase of a 1 : 10 500 mM methanol-containing SEWMs. (D) The ^{13}C NMR (151 MHz, H_2O/D_2O) δ 16.14 (C_a), 21.1 (C_b), 48.17 (C_c), 57.8 ($C_{a'}$), 81.33 (C_d), 92.04 (C_e), 169.5 (C_f), 177.8 ($C_{b'}$) on the aqueous phase of 500 mM methanol-^{13}C,d_4-containing SEWMs, which shows peak splitting for molecules where protons were replaced by deuterium. The inset details splitting patterns typical of ^{13}C–D interactions, confirming that a portion of the observed product is due to the oxidation of alcohol in the system, in addition to the breakdown of hexadecane.

products: a triplet at 1.08 ppm and a corresponding quartet at 3.56 ppm corresponding to ethanol; a singlet at 1.98 ppm corresponding to acetic acid; a singlet at 3.27 ppm corresponding to methanol; a singlet at 4.95 ppm corresponding to methanediol (hydrated form of formaldehyde); a singlet at 5.07 ppm corresponding to oxydimethanol; and, a singlet at 8.23 ppm corresponding to formic acid (Fig. 7A). Similarly, the aqueous phase obtained by the ultrasonication of 500 mM methanol-, ethanol-, and 1-propanol-containing SEWMs yielded a ^{1}H NMR spectrum (Fig. 7B, S29) featuring signals nearly identical to those observed for the alcohol-free SEWMs system. These assignments were corroborated by acquiring the ^{13}C NMR spectrum on the aqueous phase extracted after ultrasonicating 500 mM methanol-containing SEWMs (Fig. 7C). The spectrum showed a singlet at 49.25 ppm for methanol, a singlet at 17.12 ppm and 57.8 ppm for ethanol, a singlet at 82.18 ppm for methanediol, a singlet at 92.9 ppm for oxydimethanol, a singlet at 167.81 ppm for formic acid, and a singlet at 20.85 ppm and 177.24 ppm for acetic acid. Structural assignments were confirmed by spiking samples with known standards of methanol, ethanol, formic acid, and acetic acid, which resulted in a predictable increase in peak intensities (Fig. S30 and Tables S2–S5). Quantification of the identified peaks was carried out by qNMR using triphenylphosphate (TPP, 48.5 mM in $CDCl_3$) as an external calibration standard. To better elucidate the contributions of different oxidation pathways, reagent consumption and product formation were analyzed on a common molar basis using qNMR. Concentrations of remaining short-chain alcohol reagents and major oxidation products, including formic acid and acetic acid, are summarized in Fig. S31. These results demonstrate that the oxidative pathway is not limited to the primary production of hexadecanol as we have reported previously;[23] rather, it includes the formation of water-soluble small organic molecules generated *via* oxidative pathways that accumulate in the aqueous phase during ultrasonication, followed by centrifugation.

A key challenge in interpreting these results is that both the hexadecane oil phase and the short-chain alcohols can potentially oxidize into identical small-molecule products. Indeed, ^{1}H NMR spectra of the aqueous phase following the ultrasonication of alcohol-free (Fig. 7A) and alcohol-containing (methanol, ethanol, and propanol; Fig. 7B, S29) SEWMs are visually indistinguishable. To distinguish between these two oxidative pathways and definitively identify the carbon source, we

conducted isotopic labeling experiments using 500 mM of $^{13}CD_3OD$ in a SEWM, ultrasonicated under identical conditions (30 minutes, ambient gas environment), with the aqueous phase characterized using ^{13}C NMR. We observed distinct peak splitting and dual-signature in the ^{13}C NMR spectrum for oxidation products-methanol, methanediol, oxydimethanol, and formic acid (Fig. 7D). For instance, the formic acid signal at 169.5 ppm appeared as a triplet ($J_{C-D} \sim 30$ Hz) due to spin-coupling with the directly attached deuterium ($I = 1$). Notably, a distinct singlet was observed immediately adjacent to this triplet, representing the fraction of the same product derived from the unlabeled hexadecane (Fig. S32). Interestingly, the peak intensities for ethanol and acetic acid were significantly lower than those of the other products, and they appeared as singlets. This suggests that ethanol and acetic acid are primarily the oxidation products of hexadecane, while methanediol, oxydimethanol, and formic acid are produced by the oxidation of both methanol and hexadecane. This unambiguously confirms that the short-chain amphiphilic alcohols do not merely facilitate the formation of H_2O_2 and H_2 *via* reduction, but actively participate in the oxidative half-reactions. This enhanced oxidative flux likely drives the observed improvement in the corresponding reduction kinetics, maintaining the system's overall redox balance. Overall, differences in product yields across methanol, ethanol, and 1-propanol containing SEWMs may arise from variations in the kinetics of alcohol oxidation, SEWMs interfacial activity, or differing partitioning behavior. However, methanol and ethanol acted as strong modifiers for all conditions, significantly enhancing overall redox activity by producing increased amounts of oxygenated and hydrogenated products, in addition to enhancing H_2O_2 and H_2 relative to alcohol-free SEWMs. We now turn to exploring the possible molecular origins for this improved reactivity.

3.6 Molecular dynamic simulations to help explain the increased reactivity of alcohol containing SEWMs

Here, we are interested in elucidating the role of short-chain alcohols as interfacial additives in aqueous microdroplets within hexadecane. A first approach to explain the improved reactivity of alcohol-containing SEWMs potentially lies with the physicochemical properties of alcohol *vs.* water. Notably, the dielectric constant of these short-chain alcohols (32.6–20.1) is much smaller than water's dielectric constant (78.4), perhaps leading to a decrease in stability and a subsequent increase in reactivity of reactive oxygen species known to be generated in microdroplets such as $OH^{\bullet}$ and $HO_2^{\bullet}$.[23,45–47] At the same time, short-chain alcohols have a much larger electronic polarizability (3.29–6.82) than water (1.45), a property that describes the ability of the electron cloud to distort in the presence of an electric field, and therefore, which could enhance interfacial charge separation and electron transfer, also implicated in microdroplet reactivity.[21,48,49]

However, to better understand the role that the alcohols play in modulating the energetics and structure of the microdroplet water–oil interface, we turned to molecular dynamics (MD) simulations of methanol-containing and alcohol-free droplets. As shown in Fig. 8A, the MD simulations revealed that the alcohols orient themselves at the interface of the droplet. To better understand how the localized presence of alcohols near the interface might affect the reactivity of the system, we interrogated the structure of the hydrogen bonding network of water molecules at the interface located near and far away from alcohols using radial distribution functions (RDF). The interfacial water–water hydrogen bonding (HB) in methanol-containing systems is summarized in Fig. 8B. As seen, the network is highly sensitive to the presence and concentration of alcohol molecules at the interface. Our simulations indicated that the number of HB for alcohol-free systems was 3.0, a number that decreased across all methanol concentrations studied. This reduction in the number of water–water HBs suggests that methanol disrupts the local water–water HB network by competing for hydrogen-bonding partners and thereby weakens the cooperative hydrogen bond structure at the interface. The degree of disruption is concentration dependent (Fig. S33). At low concentrations of methanol, the average interfacial water–water HB per water near methanol and far away from methanol is 2.0 HB and 3.0 HB, respectively. Yet as concentration increases, the number of HB per water far away from methanol decreases, indicating a broader disruption to the overall HB network at the interface. Notably, the hydrogen bond concentration trend also follows the experimentally observed increase in redox reactivity of methanol-containing SEWMs, where higher concentrations of methanol in SEWMs experience a greater reactivity and a greater overall disruption of the interfacial water–water HB network. Such modulation of the interfacial hydrogen bond structure is expected to influence the reactivity of aqueous and alcohol-containing SEWMs, since the availability and lifetime of hydrogen bonds can affect proton transfer and radical stabilization pathways that are critical for interfacial redox chemical processes, such as the oxygen reduction reaction observed here.

We examined the hydrogen bond lifetimes to better capture the dynamic nature of the interfacial hydrogen bonding network. Our results (Fig. S34) show that interfacial water molecules near alcohols consistently exhibit longer hydrogen bond lifetimes compared to far water. This suggests that although alcohol molecules disrupt the overall connectivity of the hydrogen bond network, they simultaneously stabilize the hydrogen bonds that form within the alcohol solvation shell. Interestingly, the effect is most pronounced for longer-chain primary alcohols such as 1-butanol and 1-propanol, where near-water hydrogen bond lifetimes are significantly extended relative to far-water. This stabilization suggests that longer alkyl chains promote a more persistent local hydrogen bonding environment, likely due to their stronger interfacial partitioning and ability to anchor water molecules *via* their hydroxyl groups. A similar trend is observed when comparing alcohols within the butanol series. The order of stabilization (near alcohol) follows 1-butanol > 2-butanol > *t*-butanol > i-butanol, suggesting that primary butanol stabilizes interfacial hydrogen bonds most effectively, while secondary and branched butanol show progressively weaker effects. These differences can be attributed

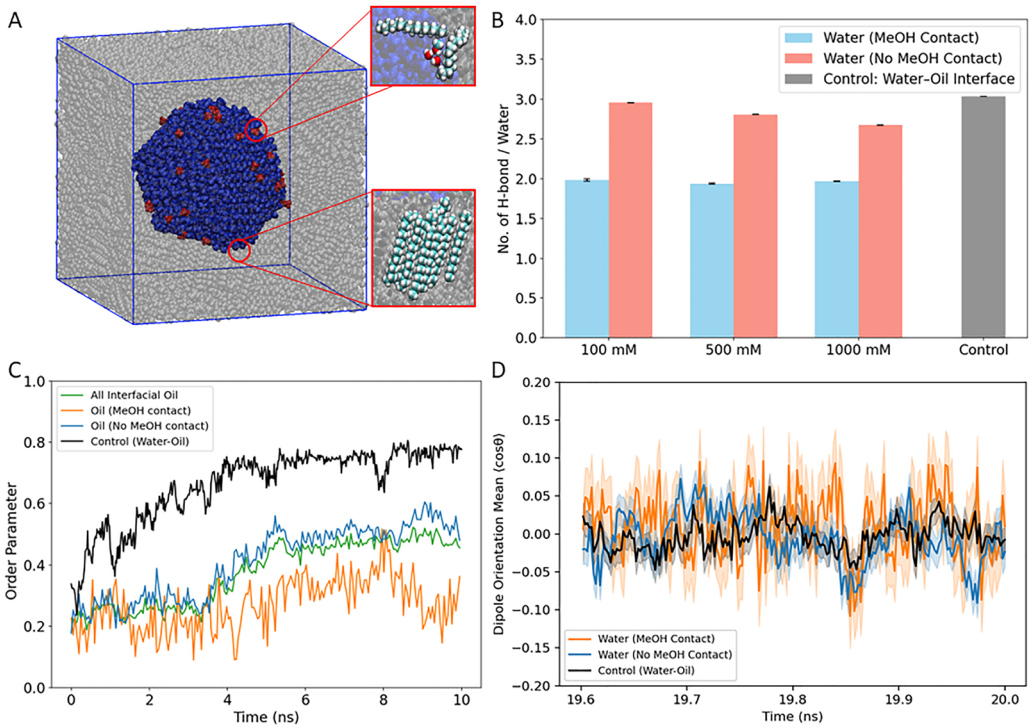

Fig. 8 Molecular dynamics simulations of alcohol-containing droplet systems and analyzed characteristics of the water–oil interface. (A) The molecular dynamics simulation of 1000 mM MeOH in hexadecane (water: orange, MeOH: red, hexadecane: gray). (B) The calculated number of water–water hydrogen bonds (W–W HB) per water molecule at the water–oil interface. Molecules are defined as interfacial if they are within 0.5 nm of hexadecane. Interfacial water molecules are determined to be near and far from interfacial alcohol molecules if they are within 0.35 nm or further than 0.35 nm from the hydrogen of the alcohol molecules, respectively. (C) The calculated interfacial hexadecane order parameter, S. (D) The average interfacial water molecule dipole orientation. A negative $\cos\theta$ represents a water molecule dipole orientation pointing inwards towards the aqueous droplet.

to steric hindrance and reduced hydrogen bond accessibility in branched alcohols, which limit the efficiency of alcohol–water interactions. Overall, these results suggest that longer primary alcohols not only disrupt the water–water network, but also increase dynamics and create longer-lived hydrogen bonds near the interface, thereby extending the residence time of interfacial water molecules. These effects provide a molecular-level explanation for the experimentally observed increase in reactivity in alcohol-containing SEWMs.

The orientation and alignment of the interfacial hexadecane were also investigated in the presence and absence of alcohols. The interfacial hexadecane results for 500 mM methanol-containing and alcohol-free droplets are summarized in Fig. 8C. An order parameter of 1 corresponds to the perfect alignment of hexadecane chains normal to the droplet surface. The order parameter of the interfacial hexadecane molecules in alcohol-free droplets is much greater than that observed in alcohol-containing ones. Additionally, hexadecane molecules near interfacial alcohol molecules exhibit an even lower order parameter regardless of alcohol concentration (Fig. S35). The disruption of interfacial molecular ordering can enhance microdroplet reactivity by increasing interfacial heterogeneity and increasing the dynamics of the interface by decreasing interfacial rigidity. Additionally, this disruption is expected to weaken the hydrogen bonding network at the interface and likely contributes to the decrease in the number of HBs calculated in Fig. 8B.

The dipole orientation of interfacial water molecules was also tracked throughout the MD simulations. As seen in Fig. 8D, interfacial water molecules near methanol molecules experience a much higher degree of dipole orientation fluctuation relative to interfacial water molecules in the alcohol-free droplet simulation. The decrease in order parameter and increase in dipole orientation fluctuation should also influence the local electric field that interfacial molecules experience. As such, we utilized these MD simulations to calculate the local electric field on individual interfacial water molecules (Fig. S36). Interfacial water molecules near methanol experience increased fluctuations and extremes in their local electric field, reaching up to 1 V nm^{-1} greater electric fields relative to water molecules far away from methanol and water molecules in methanol-free water droplets. These increased dynamics have been implicated in increasing water-in-oil microdroplet reactivity[79] and could also help explain why alcohol-containing SEWMs have increased reactivity.

4. Conclusion

In summary, short-chain, primary alcohols are demonstrated as interfacial additives for SEWMs to enhance the production of

H_2 and H_2O_2. Not only did SEWMs prepared with varying concentrations of alcohols retain the H_2 and H_2O_2 generation ability of the previously reported alcohol-free system, but also displayed distinct trends affecting the production of these chemicals. Short-chain alcohols produced the highest yields of H_2O_2 at high concentrations ($\sim$1 M) within SEWMs, while long-chain alcohols did so at low concentrations ($\sim$100 mM). Primary alcohol-containing SEWMs substantially increased the yields of both H_2O_2 and H_2 in comparison to alcohol-free and substituted alcohol-containing SEWMs. Control of the local gaseous environment further helped tune their redox selectivity. Under oxygenation, methanol-containing SEWMs produced approximately 2$\times$ the amount of H_2O_2, while in the absence of oxygen, they exhibited up to 3$\times$ the yield of H_2, compared to SEWMs operated in ambient conditions.

Complementary to the reducing conditions needed to produce H_2O_2, we firmly established oxidation reactions occurring within both the oil and aqueous phases of these alcohol-containing SEWMs. These reactions led to the formation of the gaseous products in the headspace: CO_2, CO, and CH_4, and the water-soluble, organic products in the extracted aqueous phase: mainly formic acid, acetic acid, and methanediol. Isotope labeling experiments confirmed that alcohols participated in a significant portion of the oxidation half reactions in addition to the previously reported hexadecane oxidation.[23] Complementary molecular dynamics simulations supported these experimental findings, showing that alcohols reside at the microdroplet interface, where they disrupt the local hydrogen bonding network, modify the structure and properties of the interface, and likely lower energetic barriers for interfacial redox processes. Collectively, these findings establish short-chain alcohols as a versatile handle for restructuring microdroplet interfaces, providing new routes to control and enhance microdroplet redox activity.

The simplicity of this catalyst-free system, combined with its demonstrated redox tunability, highlights SEWMs as a potentially deployable, on-demand platform for catalyst-free redox chemistry. The ability to generate and tune product distributions up to $\sim$60 mM yields of H_2O_2 within 30 minutes using only a commercial ultrasonic bath, aqueous and oil phases, and ambient atmospheric conditions, provides an on-demand alternative to the solvent-intensive, thermochemical platforms conventionally used for the generation of H_2O_2 (and possibly other gases). While the present work demonstrates the successful use of modified SEWMs to improve the generation of H_2O_2 as a model compound, future scale-up studies could evaluate the energy efficiency of SEWM-based processes relative to conventional H_2O_2 and H_2 production methods, or of any other value-added products that could engage in redox reactivity. Ongoing efforts are focused on utilizing the large quantities of H_2O_2 and H_2 produced as *in situ* chemical feedstocks for downstream, value-added chemical transformations both in the presence and absence of metal co-catalysts. More broadly, understanding how molecular additives such as alcohols can tune microdroplet redox activity provides a framework for controlling microdroplet reactivity in SEWMs and other emerging microdroplet systems at the air–water interface, enabling control of microdroplet interfacial structures and reaction pathways.

Author contributions

G. H., A. A., and J. R.-L. conceptualized the ideas. G. H. and J. R.-L. supervised the investigations. J. R.-L. acquired the funding and administered the project. G. H., S. R., E. G., and F. R. performed the core GC and UV-vis experiments. S. R. performed, visualized, and analyzed the NMR experiments. S. L. and R. S. A. developed the methodology and software for MD simulations and performed, analyzed, and visualized the simulations. G. H. curated data, developed the methodology for GC and UV-vis experiments, and performed image analysis and visualization. H. V. N. and C. S. developed the methodology for microdroplet imaging and performed their visualization and analysis. G. H. and H. V. N. performed the microdroplet imaging experiments. G. H., S. L., S. R., and J. R.-L. wrote the original draft. All authors were involved in editing and approving the final version of the manuscript.

Conflicts of interest

We declare no conflicts of interest.

Data availability

The data supporting this article have been included as part of the supplementary information (SI). The original raw datasets for all microdroplet imaging, GC, UV-Vis, and NMR experiments are available within the SI. Supplementary information is available. See DOI: https://doi.org/10.1039/d6ey00123h.

For additional information about the MD simulations, please contact Rajeev S. Assary.

Acknowledgements

This material is based upon work supported by the U.S. Department of Energy, Office of Science, Science Foundations for Energy Earthshots Program, under Award Number DE-SC0024892. Disclaimer: ‘‘This report was prepared as an account of work sponsored by an agency of the United States Government. Neither the United States Government nor any agency thereof, nor any of their employees, makes any warranty, express or implied, or assumes any legal liability or responsibility for the accuracy, completeness, or usefulness of any information, apparatus, product, or process disclosed, or represents that its use would not infringe privately owned rights. Reference herein to any specific commercial product, process, or service by trade name, trademark, manufacturer, or otherwise does not necessarily constitute or imply its endorsement, recommendation, or favoring by the United States Government or any agency thereof. The views and opinions of authors expressed herein do not necessarily state or reflect those of the United States Government or any agency thereof.’’

This material is based upon work supported by the Air Force Office of Scientific Research under award number FA9550-25-C-B010 in the amount of $143,000. G. H. gratefully acknowledges the financial support from the Robert C. and Carolyn J. Springborn Endowment and support by the Department of Defense (DoD) through the National Defense Science & Engineering Graduate (NDSEG) Fellowship Program. We thank Lingyang Zhu and the University of Illinois School of Chemical Sciences (SCS) nuclear magnetic resonance (NMR) laboratory for assistance with NMR spectroscopy. The authors thank Yichen Li for his help with designing the 3D printed parts used during this project.

References

1 R. Hage and A. Lienke, Applications of Transition-Metal Catalysts to Textile and Wood-Pulp Bleaching, *Angew. Chem., Int. Ed.*, 2006, **45**(2), 206–222, DOI: 10.1002/anie.200500525.

2 P. Tundo, P. Anastas, D. S. Black, J. Breen, T. J. Collins and S. Memoli, *et al.*, Synthetic pathways and processes in green chemistry. Introductory overview, *Pure Appl. Chem.*, 2000, **72**(7), 1207–1228, DOI: 10.1351/pac200072071207.

3 M. Hey, Paper Bleaching: Its Simple Chemistry and Working Procedures, *Pap. Conserv.*, 1977, **2**(1), 10–23, DOI: 10.1080/03094227.1977.9638494.

4 R. Ciriminna, L. Albanese, F. Meneguzzo and M. Pagliaro, Hydrogen Peroxide: A Key Chemical for Today's Sustainable Development, *ChemSusChem*, 2016, **9**(24), 3374–3381, DOI: 10.1002/cssc.201600895.

5 C. W. Jones, in *Applications of Hydrogen Peroxide and Derivatives [Internet]*, ed. J. H. Clark and M. J. Braithwaite, The Royal Society of Chemistry, 1999. , DOI: 10.1039/9781847550132.

6 V. Russo, R. Tesser, E. Santacesaria and M. Di Serio, Chemical and Technical Aspects of Propene Oxide Production *via* Hydrogen Peroxide (HPPO Process), *Ind. Eng. Chem. Res.*, 2013, **52**(3), 1168–1178, DOI: 10.1021/ie3023862.

7 M. Uyanik and K. Ishihara, Baeyer–Villiger Oxidation Using Hydrogen Peroxide, *ACS Catal.*, 2013, **3**(4), 513–520, DOI: 10.1021/cs300821u.

8 W. Eul, A. Moeller, N. Steiner and U. Staff, Hydrogen Peroxide, *Kirk-Othmer Encyclopedia of Chemical Technology [Internet]*, John Wiley & Sons, Ltd, 2026. pp. 1–43. Available from: https://onlinelibrary.wiley.com/doi/abs/10.1002/0471238961.0825041808051919.a01.pub3, DOI: 10.1002/0471238961.0825041808051919.a01.pub3.

9 T. Nishimi, T. Kamachi, K. Kato, T. Kato and K. Yoshizawa, Mechanistic Study on the Production of Hydrogen Peroxide in the Anthraquinone Process, *Eur. J. Org. Chem.*, 2011, (22), 4113–4120, DOI: 10.1002/ejoc.201100300.

10 G. Goor, J. Glenneberg, S. Jacobi, J. Dadabhoy and E. Candido, Hydrogen Peroxide, *Ullmann's Encyclopedia of Industrial Chemistry [Internet]*, John Wiley & Sons, Ltd, 2019, pp. 443–466. Available from: https://onlinelibrary.wiley.com/doi/abs/10.1002/14356007.a13_443.pub3, DOI: 10.1002/14356007.a13_443.pub3.

11 J. R. Kirchner, Hydrogen Peroxide, *Kirk-Othmer Encyclopedia of Chemical Technology*, John Wiley & Sons, Ltd, New York, NY, 3rd edn, 1979, pp. 12–38.

12 IEA [Internet]. 2025 [cited 2026 May 13]. Global Hydrogen Review 2025 – Analysis. Available from: https://www.iea.org/reports/global-hydrogen-review-2025.

13 N. Rambhujun, M. S. Salman, T. Wang, C. Pratthana, P. Sapkota and M. Costalin, *et al.*, Renewable hydrogen for the chemical industry, *MRS Energy Sustainability*, 2020, **7**(1), 33, DOI: 10.1557/mre.2020.33.

14 S. A. Ansari, M. W. Alam, N. Dhanda, M. S. Abbasi, M. E. Ahmed and A. B. Alrashidi, *et al.*, Sustainable Hydrogen Production, a Review of Methods, Types, Applications, Challenges, and Future Perspectives, *Global Challenges*, 2025, **9**(6), 2500086, DOI: 10.1002/gch2.202500086.

15 C. Gunathilake, I. Soliman, D. Panthi, P. Tandler, O. Fatani and N. A. Ghulamullah, *et al.*, A comprehensive review on hydrogen production, storage, and applications, *Chem. Soc. Rev.*, 2024, **53**(22), 10900–10969, DOI: 10.1039/D3CS00731F.

16 F. Qureshi, M. Yusuf, M. Arham Khan, H. Ibrahim, B. C. Ekeoma and H. Kamyab, *et al.*, A State-of-The-Art Review on the Latest trends in Hydrogen production, storage, and transportation techniques, *Fuel*, 2023, **340**, 127574, DOI: 10.1016/j.fuel.2023.127574.

17 A. Boyano, A. M. Blanco-Marigorta, T. Morosuk and G. Tsatsaronis, Exergoenvironmental analysis of a steam methane reforming process for hydrogen production, *Energy*, 2011, **36**(4), 2202–2214, DOI: 10.1016/j.energy.2010.05.020; 5th Dubrovnik Conference on Sustainable Development of Energy, Water & Environment Systems.

18 J. M. Campos-Martin, G. Blanco-Brieva and J. L. G. Fierro, Hydrogen Peroxide Synthesis: An Outlook beyond the Anthraquinone Process, *Angew. Chem., Int. Ed.*, 2006, **45**(42), 6962–6984, DOI: 10.1002/anie.200503779.

19 Z. Mohammadi, S. Allahyari, S. Rahimi, M. Fathi, S. Mohammadi and A. H. Mosaffa, Comprehensive review of hydrogen production technologies, pathways, and applications for advancing global sustainable energy goals, *Energy Convers. Manage.:X*, 2025, **28**, 101319, DOI: 10.1016/j.ecmx.2025.101319.

20 J. P. Heindel, H. Hao, R. A. LaCour and T. Head-Gordon, Spontaneous Formation of Hydrogen Peroxide in Water Microdroplets, *J. Phys. Chem. Lett.*, 2022, **13**(43), 10035–10041, DOI: 10.1021/acs.jpclett.2c01721.

21 X. Chen, Y. Xia, Y. Wu, Y. Xu, X. Jia and R. N. Zare, *et al.*, Sprayed Oil–Water Microdroplets as a Hydrogen Source, *J. Am. Chem. Soc.*, 2024, **146**(15), 10868–10874, DOI: 10.1021/jacs.4c01455.

22 J. K. Lee, K. L. Walker, H. S. Han, J. Kang, F. B. Prinz and R. M. Waymouth, *et al.*, Spontaneous generation of hydrogen peroxide from aqueous microdroplets, *Proc. Natl. Acad. Sci. U. S. A.*, 2019, **116**(39), 19294–19298, DOI: 10.1073/pnas.1911883116.

23 A. Asserghine, A. Baby, J. N'Diaye, A. I. B. Romo, S. Das and C. A. Litts, *et al.*, Dissolved Oxygen Redox as the Source of

Hydrogen Peroxide and Hydroxyl Radical in Sonicated Emulsive Water Microdroplets, *J. Am. Chem. Soc.*, 2025, **147**(14), 11851–11858, DOI: 10.1021/jacs.4c16759.

24 K. S. Suslick, Sonochemistry, *Science*, 1990, **247**(4949), 1439–1445, DOI: 10.1126/science.247.4949.1439.

25 S. Kentish and M. Ashokkumar The Physical and Chemical Effects of Ultrasound, in ed. *Ultrasound Technologies for Food and Bioprocessing [Internet]*, H. Feng, G. Barbosa-Canovas and J. Weiss, Springer, New York, NY, 2011, pp. 1–12. , DOI: 10.1007/978-1-4419-7472-3_1.

26 W. Duco, V. Grosso, D. Zaccari and A. T. Soltermann, Generation of ROS mediated by mechanical waves (ultrasound) and its possible applications, *Methods*, 2016, **109**, 141–148, DOI: 10.1016/j.ymeth.2016.07.015; Current Methods to unravel Reactive Oxygen Species (ROS) Biology.

27 J. Chandrapala, C. Oliver, S. Kentish and M. Ashokkumar, Ultrasonics in food processing, *Ultrason. Sonochem.*, 2012, **19**(5), 975–983, DOI: 10.1016/j.ultsonch.2012.01.010.

28 M. R. Hoffmann, I. Hua and R. Höchemer, Application of ultrasonic irradiation for the degradation of chemical contaminants in water, *Ultrason. Sonochem.*, 1996, **3**(3), S163–S172, DOI: 10.1016/S1350-4177(96)00022-3; Proceedings of the Symposium on the Chemical Effects of Ultrasound in the 1995 International Chemical Congress of Pacific Basin Societies.

29 M. Goel, H. Hongqiang, A. S. Mujumdar and M. B. Ray, Sonochemical decomposition of volatile and non-volatile organic compounds—a comparative study, *Water Res.*, 2004, **38**(19), 4247–4261, DOI: 10.1016/j.watres.2004.08.008.

30 H. Destaillats, H. M. Hung and M. R. Hoffmann, Degradation of Alkylphenol Ethoxylate Surfactants in Water with Ultrasonic Irradiation, *Environ. Sci. Technol.*, 2000, **34**(2), 311–317, DOI: 10.1021/es990384x.

31 Y. T. Didenko and K. S. Suslick, Chemical aerosol flow synthesis of semiconductor nanoparticles, *J. Am. Chem. Soc.*, 2005, **127**(35), 12196–12197, DOI: 10.1021/ja054124t PubMed PMID: 16131177.

32 S. E. Skrabalak and K. S. Suslick, Porous Carbon Powders Prepared by Ultrasonic Spray Pyrolysis, *J. Am. Chem. Soc.*, 2006, **128**(39), 12642–12643, DOI: 10.1021/ja064899h.

33 J. Sheen, J. Shin and J. K. Lee, Interfacial redox chemistry-driven formation and inhibition of nanoparticles in ultrasonic-humidifier microdroplets, *Environ. Sci.: Nano*, 2025, **12**(12), 5177–5184, DOI: 10.1039/d5en00741k.

34 J. H. Bang and K. S. Suslick, Applications of ultrasound to the synthesis of nanostructured materials, *Adv. Mater.*, 2010, **22**(10), 1039–1059, DOI: 10.1002/adma.200904093 PubMed PMID: 20401929.

35 X. Zhou, S. Du, W. Zhang and B. Zheng, Deciphering the mechanism of hydrogen peroxide formation in ultrasound-mediated water-in-oil microdroplets, *Chem. Sci.*, 2025, **16**(15), 6450–6457, DOI: 10.1039/d4sc08098j.

36 K. Lee, M. A. Mehrgardi and R. N. Zare, Interfacial Curvature, not Simply Size, Controls Spontaneous Hydrogen Peroxide Formation in Water Microdroplets, *J. Am. Chem. Soc.*, 2025, **147**(36), 33240–33247, DOI: 10.1021/jacs.5c11575.

37 S. Bose, K. Lee, S. Q. Choi and R. N. Zare, Harnessing Oil–Water Microinterfaces for the Catalyst-Free Oxidative Degradation of Toxic Organic Pollutants, *J. Am. Chem. Soc.*, 2026, **148**(21), 22209–22218, DOI: 10.1021/jacs.6c05344.

38 X. Chen, Y. Xia, Z. Zhang, L. Hua, X. Jia and F. Wang, *et al.*, Hydrocarbon Degradation by Contact with Anoxic Water Microdroplets, *J. Am. Chem. Soc.*, 2023, **145**(39), 21538–21545, DOI: 10.1021/jacs.3c07445.

39 K. Lee, H. R. Lee, Y. H. Kim, J. Park, S. Cho and S. Li, *et al.*, Microdroplet-Mediated Radical Polymerization, *ACS Cent. Sci.*, 2022, **8**(9), 1265–1271, DOI: 10.1021/acscentsci.2c00694 PubMed PMID: 36188353; PubMed Central PMCID: PMC9523774.

40 M. A. Eatoo and H. Mishra, Busting the myth of spontaneous formation of H2O2 at the air–water interface: contributions of the liquid–solid interface and dissolved oxygen exposed, *Chem. Sci.*, 2024, **15**(9), 3093–3103, DOI: 10.1039/D3SC06534K.

41 M. A. Eatoo and H. Mishra, Disentangling the Roles of Dissolved Oxygen, Common Salts, and pH on Spontaneous Hydrogen Peroxide Production in Water: No O2, No H2O2, *J. Am. Chem. Soc.*, 2025, **147**(39), 35392–35400, DOI: 10.1021/jacs.5c09028.

42 Z. Wei, Y. Li, R. G. Cooks and X. Yan, Accelerated Reaction Kinetics in Microdroplets: Overview and Recent Developments, *Annu. Rev. Phys. Chem.*, 2020, **71**, 31–51, DOI: 10.1146/annurev-physchem-121319-110654.

43 X. Yan, R. M. Bain and R. G. Cooks, Organic Reactions in Microdroplets: Reaction Acceleration Revealed by Mass Spectrometry, *Angew. Chem., Int. Ed.*, 2016, **55**(42), 12960–12972, DOI: 10.1002/anie.201602270.

44 Y. Jung and R. A. Marcus, On the Theory of Organic Catalysis ‘‘on Water, *J. Am. Chem. Soc.*, 2007, **129**(17), 5492–5502, DOI: 10.1021/ja068120f.

45 H. Xiong, J. K. Lee, R. N. Zare and W. Min, Strong Electric Field Observed at the Interface of Aqueous Microdroplets, *J. Phys. Chem. Lett.*, 2020, **11**(17), 7423–7428, DOI: 10.1021/acs.jpclett.0c02061.

46 D. Zhang, X. Yuan, C. Gong and X. Zhang, High Electric Field on Water Microdroplets Catalyzes Spontaneous and Ultrafast Oxidative C–H/N–H Cross-Coupling, *J. Am. Chem. Soc.*, 2022, **144**(35), 16184–16190, DOI: 10.1021/jacs.2c07385.

47 C. Zhu, L. N. Pham, X. Yuan, H. Ouyang, M. L. Coote and X. Zhang, High Electric Fields on Water Microdroplets Catalyze Spontaneous and Fast Reactions in Halogen-Bond Complexes, *J. Am. Chem. Soc.*, 2023, **145**(39), 21207–21212, DOI: 10.1021/jacs.3c08818.

48 B. Chen, Y. Xia, R. He, H. Sang, W. Zhang and J. Li, *et al.*, Water–solid contact electrification causes hydrogen peroxide production from hydroxyl radical recombination in sprayed microdroplets, *Proc. Natl. Acad. Sci. U. S. A.*, 2022, **119**(32), e2209056119, DOI: 10.1073/pnas.2209056119.

49 A. Berbille, X. F. Li, Y. Su, S. Li, X. Zhao and L. Zhu, *et al.*, Mechanism for Generating H2O2 at Water-Solid Interface

by Contact-Electrification, *Adv. Mater.*, 2023, **35**(46), 2304387, DOI: 10.1002/adma.202304387.
50 J. Li, C. Liu, H. Chen and R. N. Zare, Accelerated Oxidation of Organic Sulfides by Microdroplet Chemistry, *J. Org. Chem.*, 2021, **86**(7), 5011–5015, DOI: 10.1021/acs.joc.0c02942.
51 K. Lee, Y. Cho, J. C. Kim, C. Choi, J. Kim and J. K. Lee, *et al.*, Catalyst-free selective oxidation of C(sp3)-H bonds in toluene on water, *Nat. Commun.*, 2024, **15**(1), 6127, DOI: 10.1038/s41467-024-50352-7 PubMed PMID: 39033208; PubMed Central PMCID: PMC11271591.
52 S. Banerjee and R. N. Zare, Syntheses of Isoquinoline and Substituted Quinolines in Charged Microdroplets, *Angew. Chem., Int. Ed.*, 2015, **54**(49), 14795–14799, DOI: 10.1002/anie.201507805 PubMed PMID: 26450661.
53 X. Yan, H. Cheng and R. N. Zare, Two-Phase Reactions in Microdroplets without the Use of Phase-Transfer Catalysts, *Angew. Chem., Int. Ed.*, 2017, **56**(13), 3562–3565, DOI: 10.1002/anie.201612308 PubMed PMID: 28225181.
54 X. Song, C. Basheer and R. N. Zare, Making ammonia from nitrogen and water microdroplets, *Proc. Natl. Acad. Sci. U. S. A.*, 2023, **120**(16), e2301206120, DOI: 10.1073/pnas.2301206120 PubMed PMID: 37036968; PubMed Central PMCID: PMC10120050.
55 X. Zheng, Y. G. Fang, M. Tan, B. Chen, J. S. Francisco and C. Zhu, *et al.*, Accelerated Methane Photo-oxidation at the Air–Water Interface, *J. Am. Chem. Soc.*, 2025, **147**(30), 26635–26642, DOI: 10.1021/jacs.5c06925.
56 L. Zhao, X. Song, C. Gong, D. Zhang, R. Wang and R. N. Zare, *et al.*, Sprayed water microdroplets containing dissolved pyridine spontaneously generate pyridyl anions, *Proc. Natl. Acad. Sci. U. S. A.*, 2022, **119**(12), e2200991119, DOI: 10.1073/pnas.2200991119.
57 A. Kumar, S. Mondal, M. Mofidfar, R. N. Zare and S. Banerjee, Capturing Reactive Carbanions by Microdroplets, *J. Am. Chem. Soc.*, 2022, **144**(17), 7573–7577, DOI: 10.1021/jacs.2c01577.
58 I. Nam, J. K. Lee, H. G. Nam and R. N. Zare, Abiotic production of sugar phosphates and uridine ribonucleoside in aqueous microdroplets, *Proc. Natl. Acad. Sci. U. S. A.*, 2017, **114**(47), 12396–12400, DOI: 10.1073/pnas.1714896114.
59 I. Nam, H. G. Nam and R. N. Zare, Abiotic synthesis of purine and pyrimidine ribonucleosides in aqueous microdroplets, *Proc. Natl. Acad. Sci. U. S. A.*, 2018, **115**(1), 36–40, DOI: 10.1073/pnas.1718559115.
60 M. Girod, E. Moyano, D. I. Campbell and R. G. Cooks, Accelerated bimolecular reactions in microdroplets studied by desorption electrospray ionization mass spectrometry, *Chem. Sci.*, 2011, **2**(3), 501–510, DOI: 10.1039/C0SC00416B.
61 A. K. Badu-Tawiah, D. I. Campbell and R. G. Cooks, Accelerated C–N Bond Formation in Dropcast Thin Films on Ambient Surfaces, *J. Am. Soc. Mass Spectrom.*, 2012, **23**(9), 1461–1468, DOI: 10.1007/s13361-012-0394-y.
62 T. Müller, A. Badu-Tawiah and R. G. Cooks, Accelerated carbon-carbon bond-forming reactions in preparative electrospray, *Angew. Chem., Int. Ed.*, 2012, **51**(47), 11832–11835, DOI: 10.1002/anie.201206632 PubMed PMID: 23042619.
63 R. M. Bain, C. J. Pulliam and R. G. Cooks, Accelerated Hantzsch electrospray synthesis with temporal control of reaction intermediates, *Chem. Sci.*, 2014, **6**(1), 397–401, DOI: 10.1039/C4SC02436B.
64 G. Yuan, Z. Jin, Y. Cao, H. M. Schulz, J. Gluyas and K. Liu, *et al.*, Microdroplets initiate organic-inorganic interactions and mass transfer in thermal hydrous geosystems, *Nat. Commun.*, 2024, **15**(1), 4960, DOI: 10.1038/s41467-024-49293-y.
65 D. R. Heiss and A. K. Badu-Tawiah, In-Source Microdroplet Derivatization Using Coaxial Contained-Electrospray Mass Spectrometry for Enhanced Sensitivity in Saccharide Analysis, *Anal. Chem.*, 2021, **93**(50), 16779–16786, DOI: 10.1021/acs.analchem.1c02897.
66 D. S. Kulyk, C. F. Miller and A. K. Badu-Tawiah, Reactive Charged Droplets for Reduction of Matrix Effects in Electrospray Ionization Mass Spectrometry, *Anal. Chem.*, 2015, **87**(21), 10988–10994, DOI: 10.1021/acs.analchem.5b02943.
67 S. Chen, X. Li, Y. G. Fang, X. Liu, Y. Yao and B. Chen, *et al.*, Accelerated Fatty Acid Oxidation Occurs at the Water–Air Interface of Sea Spray Microdroplets, *J. Am. Chem. Soc.*, 2025, **147**(42), 38609–38614, DOI: 10.1021/jacs.5c12716.
68 M. Angelaki, Y. Carreira Mendes Da Silva, S. Perrier and C. George, Quantification and Mechanistic Investigation of the Spontaneous H2O2 Generation at the Interfaces of Salt-Containing Aqueous Droplets, *J. Am. Chem. Soc.*, 2024, **146**(12), 8327–8334, DOI: 10.1021/jacs.3c14040.
69 H. Zhang, Y. Xu, X. Fan, Y. Wang, J. Zhao and L. Qiao, *et al.*, Effect of Halide Ions on Single-Electron Oxidation Reactions in Microdroplets, *J. Phys. Chem. Lett.*, 2026, **17**(1), 355–360, DOI: 10.1021/acs.jpclett.5c03053.
70 J. Zhang, Z. Liu, C. Zhu, S. Wang, S. Zhu and C. Zhu, *et al.*, Ion-Specific Interfacial Electric Fields on Water Microdroplets for Tuning Menshutkin Reactions, *J. Am. Chem. Soc.*, 2025, **147**(42), 38428–38434, DOI: 10.1021/jacs.5c11766.
71 M. Angelaki, J. d'Erceville, D. J. Donaldson and C. George, pH Affects the Spontaneous Formation of H2O2 at the Air–Water Interfaces, *J. Am. Chem. Soc.*, 2024, **146**(38), 25889–25893, DOI: 10.1021/jacs.4c07356.
72 J. Choi, S. Yoon and Y. Son, Effects of alcohols and dissolved gases on sonochemical generation of hydrogen in a 300 kHz sonoreactor, *Ultrason. Sonochem.*, 2023, **101**, 106660, DOI: 10.1016/j.ultsonch.2023.106660.
73 H. J. C. Berendsen, D. van der Spoel and R. van Drunen, GROMACS: A message-passing parallel molecular dynamics implementation, *Comput. Phys. Commun.*, 1995, **91**(1), 43–56, DOI: 10.1016/0010-4655(95)00042-E.
74 W. L. Jorgensen, D. S. Maxwell and J. Tirado-Rives, Development and Testing of the OPLS All-Atom Force Field on Conformational Energetics and Properties of Organic Liquids, *J. Am. Chem. Soc.*, 1996, **118**(45), 11225–11236, DOI: 10.1021/ja9621760.
75 I. Yungerman, I. Starodumov, A. Fulati, K. Uto, M. Ebara and Y. Moskovitz, Full-Atomistic Optimized Potentials for

Liquid Simulations and Polymer Consistent Force Field Models for Biocompatible Shape-Memory Poly(ε-caprolactone), *J. Phys. Chem. B*, 2022, **126**(21), 3961–3972, DOI: 10.1021/acs.jpcb.2c01973.

76 M. J. Frisch, G. W. Trucks, H. B. Schlegel, G. E. Scuseria, M. A. Robb, J. R. Cheeseman, *et al.*, *Gaussian 16 Rev. C.01.*, Wallingford, CT, 2016.

77 R. Gowers, M. Linke, J. Barnoud, T. Reddy, M. Melo, S. Seyler, *et al.*, *MDAnalysis: A Python Package for the Rapid Analysis of Molecular Dynamics Simulations*, Austin, Texas, 2016, pp. 98–105. Available from: https://doi.curvenote.com/10.25080/Majora-629e541a-00e, DOI: 10.25080/Majora-629e541a-00e.

78 K. S. Suslick, J. J. Gawienowski, P. F. Schubert and H. H. Wang, Alkane sonochemistry, *J. Phys. Chem.*, 1983, **87**(13), 2299–2301, DOI: 10.1021/j100236a013.

79 L. Shi, R. A. LaCour, N. Qian, J. P. Heindel, X. Lang and R. Zhao, *et al.*, Water structure and electric fields at the interface of oil droplets, *Nature*, 2025, **640**(8057), 87–93, DOI: 10.1038/s41586-025-08702-y.